

MAGNETICALLY LEVITATED ACCELEROMETER DESIGN

A THESIS SUBMITTED TO
THE GRADUATE SCHOOL OF NATURAL AND APPLIED SCIENCES
OF
MIDDLE EAST TECHNICAL UNIVERSITY

BY

İLKE CEYLAN

IN PARTIAL FULFILLMENT OF THE REQUIREMENTS
FOR
THE DEGREE OF MASTER OF SCIENCE
IN
MECHANICAL ENGINEERING

SEPTEMBER 2019

Approval of the thesis:

MAGNETICALLY LEVITATED ACCELEROMETER DESIGN

submitted by **İLKE CEYLAN** in partial fulfillment of the requirements for the degree of **Master of Science in Mechanical Engineering Department, Middle East Technical University** by,

Prof. Dr. Halil Kalıpçılar
Dean, Graduate School of **Natural and Applied Sciences**

Prof. Dr. M. A. Sahir Arıkan
Head of Department, **Mechanical Engineering**

Assist. Prof. Dr. Kıvanç Azgın
Supervisor, **Mechanical Engineering, METU**

Examining Committee Members:

Prof. Dr. R. Tuna Balkan
Mechanical Engineering, METU

Assist. Prof. Dr. Kıvanç Azgın
Mechanical Engineering, METU

Prof. Dr. Erhan İlhan Konukseven
Mechanical Engineering, METU

Assist. Prof. Dr. Ali Emre Turgut
Mechanical Engineering, METU

Assist. Prof. Dr. Emir Kutluay
Mechanical Engineering, Hacettepe University

Date: 09.09.2019

I hereby declare that all information in this document has been obtained and presented in accordance with academic rules and ethical conduct. I also declare that, as required by these rules and conduct, I have fully cited and referenced all material and results that are not original to this work.

Name, Surname: İlke Ceylan

Signature:

ABSTRACT

MAGNETICALLY LEVITATED ACCELEROMETER DESIGN

Ceylan, İlke
Master of Science, Mechanical Engineering
Supervisor: Assist. Prof. Dr. Kıvanç Azgın

September 2019, 90 pages

This thesis proposes the utilization of magnetic levitation for designing an acceleration sensor, taking the advantage of up-to-date contactless displacement sensing technology. The accelerometer is expected to have long-term robustness by isolating the proof mass from the rest of the accelerometer body, virtually eliminating mechanical friction and wear. Furthermore, levitated sensors have a great potential to achieve high precision. In this context, this study presents designing a levitated accelerometer, which suspends the proof mass and controls its position relative to the sensor body. When the sensor body moves, the shift of the proof mass with respect to the sensor body is detected and the control system produces feedback forces on the proof mass to keep the proof mass stationary with respect to the sensor body.

In this study, a magnetically levitated accelerometer is designed, constructed and tested. Permanent magnets are used to offset the weight of the levitated proof mass. However, that is not enough to keep it steady and stable afloat. Hence, active magnetic actuation is utilized not only for levitation but also for position control of the proof mass.

In the design phase, a mathematical model of the system is developed and a simulation model is built by using MATLAB®/Simulink®. Magnetic analyses are performed by

using finite element method. PID controllers run independently in a digital microcontroller for position control in two axes and two rotations. Eddy current sensors are installed on the system to measure the relative position along those axes. Moreover, motor drivers are used to feed the proportional current to electromagnets and evaluate the current values on the solenoids by built in sensors. Tests are conducted in order to tune the controllers and finally compare the acceleration measurements with a commercial sensor. The measurement limit of accelerometer is measured as ± 0.6 g. Bias instability and velocity random walk values is calculated as 0.174 mg and 0.182 m/s/ \sqrt{h} respectively.

Keywords: Accelerometer, Magnetic Levitation, Inertial Sensor, Active Magnetic Actuation, Stabilization

ÖZ

MANYETİK KALDIRMA KUVVETİ YARDIMIYLA İVMEÖLÇER TASARIMI

Ceylan, İlke
Yüksek Lisans, Makina Mühendisliği
Tez Danışmanı: Dr. Öğr. Üyesi Kıvanç Azgın

Eylül 2019, 90 sayfa

Bu tez, güncel temassız yer değiştirme algılama teknolojisinden yararlanarak, bir ivmeölçer tasarımı için manyetik havaya kaldırmanın kullanımını incelemeyi önermektedir. Sismik kütleyi sensörün geri kalanından izole ederek, mekanik sürtünme ve aşınmayı neredeyse ortadan kaldırarak ivmeölçerin uzun vadeli sağlamlığa sahip olması beklenir. Ayrıca, temassız sensörler yüksek hassasiyetli ölçümler elde etmek için büyük bir potansiyele sahiptir. Bu bağlamda, bu çalışma, sismik kütleyi askıda tutan ve sensör gövdesine göre konumunu kontrol eden havaya kaldırma teknolojisini kullanan bir ivmeölçer tasarlamayı sunmaktadır. Sensör gövdesi hareket ettiğinde, sismik kütlelerinin gövdeye göre yer değiştirmesi algılanır ve kontrol sistemi sismik kütleyi gövdeye göre sabit tutmak için geri besleme kuvvetleri oluşturur.

Bu çalışmada manyetik olarak havalandırılmış bir ivmeölçer tasarlanmış, inşa edilmiş ve test edilmiştir. Doğal mıknatıslar, sismik kütlelerin ağırlığını dengelemek için kullanılır. Ancak, havada sabit durması ve sabit kalması için bu yeterli değildir. Bu nedenle, aktif manyetik aktivasyon sadece havaya kaldırmak için değil aynı zamanda sismik kütlelerinin pozisyon kontrolü için de kullanılır.

Tasarım aşamasında, sistemin matematiksel bir modeli geliştirilmiştir ve MATLAB® / Simulink® kullanılarak bir benzetim modeli oluşturulmuştur. Manyetik analizler, sonlu elemanlar yöntemi kullanılarak yapılmıştır. PID kontrol methodu, iki eksen ve iki rotasyonda konum kontrolü için bağımsız olarak dijital bir mikro kontrolörde çalışmaktadır. Bu eksenler arasındaki bağıl konumu ölçmek için Eddy akım sensörleri sisteme monte edilmiştir. Dahası, motor sürücüleri, oransal akımı elektromıknatlara beslemek ve solenoidler üzerindeki akım değerlerini yerleşik sensörler tarafından değerlendirmek için kullanılmıştır. Kontrol parametrelerini ayarlamak ve son olarak ivme ölçümlerini ticari bir sensörle karşılaştırmak için testler yapılmıştır. İvmeölçerin ölçüm sınırı ± 0.6 g olarak ölçülmüştür. Eğilimdeki dengesizlik ve hız rastgele yürüme değerleri sırasıyla 0.174 mg ve 0.182 m/s/ \sqrt{h} olarak hesaplanmıştır.

Anahtar Kelimeler: İvmeölçer, Manyetik Kaldırma Yöntemi, Ataletsel Sensörler, Aktif Manyetik Eyleyici, Stabilizasyon, Levitasyon

To My Family And To My Love Burcu

ACKNOWLEDGEMENTS

First of all, I would like to thank my supervisor Assist. Prof. Dr. Kıvanç Azgın who made this work possible. His friendly guidance and expert advice have been invaluable throughout all the stages of the work. It is privilege for me to work with him.

Although I know that there is no way to express my gratitude, I would also like to thank Onur Cem Erdoğan, for being a helpful lab partner.

I would like to express my appreciation to my colleague Hayrettin Ulaş Akova for his friendship, valuable support and motivation.

I would especially like to thank my love, Burcu Eryılmaz, who stand by me through all my travails, my absences, my fits of pique and impatience. The joy that we shared made everything much easier.

Last but not least, I am very grateful to my mother, Yurdanur, my father, Cengiz and my sweet sister, İdil for their endless love, support and encouragement in all aspects of my life. Any thank would be an understatement.

TABLE OF CONTENTS

ABSTRACT	v
ÖZ.....	vii
ACKNOWLEDGEMENTS	x
TABLE OF CONTENTS	xi
LIST OF TABLES	xiv
LIST OF FIGURES	xv
LIST OF ABBREVIATIONS	xviii
LIST OF SYMBOLS	xix
CHAPTERS	
1. INTRODUCTION	1
1.1. Motivation	1
1.2. Acceleration Sensors	3
1.2.1. Scope of Application	3
1.2.2. Basic Operational Principle	4
1.2.3. Types of Accelerometers	5
1.3. Magnetic Levitation	7
1.4. Thesis Organization.....	9
2. ACTIVE MAGNETIC BEARING.....	11
2.1. Analysis of Magnetic Bearing	12
2.2. Stabilization Analysis of Active Magnetic Bearings	15
2.2.1. Unstable Force Component	15
2.2.2. State Space Representation.....	18

2.3. Controller Selection	20
3. EXPERIMENTAL SETUP	23
3.1. Components of the Setup	23
3.1.1. Electromagnetic Actuators	23
3.1.2. Permanent Magnets	25
3.1.2.1. Ferrite Permanent Magnets	25
3.1.2.2. Neodymium Magnets.....	26
3.1.3. Position Sensors	27
3.1.4. Processor	31
3.1.5. Power Amplifier	32
3.1.6. Buffer IC.....	33
3.2. Test Setup.....	35
3.3. Mechanical Dynamics.....	38
3.3.1. Equation of Motion	39
3.3.2. Magnetic Force Component Analysis	41
3.3.3. Controller Design	46
3.4. Simulations.....	48
4. PERFORMANCE EVALUATION	57
4.1. Software Design for the Processor.....	57
4.1.1. Controller Implementation	57
4.1.2. Communication with DSP Board	60
4.2. Tuning of the PID Controller	62
4.3. Comparison with a Commercial Sensor.....	66
4.3.1. STIM300 Acceleration Sensor	66

4.3.2. Tests with STIM300 and Designed Accelerometer	67
4.4. Measurement Limit	68
4.5. Allan Variance of the Test Setup.....	70
4.6. Frequency Test	74
5. SUMMARY, CONCLUSION AND FUTURE WORK.....	79
5.1. Summary of Thesis.....	79
5.2. Conclusion of the Study	80
5.3. Future Work	81
REFERENCES.....	83
A. Script for Allan Variance	87

LIST OF TABLES

TABLES

Table 1.1. Comparison of accelerometer types [10].	6
Table 3.1. Characteristics of C8 ferrite permanent magnet [17]	26
Table 3.2. Characteristic of N45 neodymium permanent magnet [18].	27
Table 4.1. Parameters of STIM300 IMU [26].	66

LIST OF FIGURES

FIGURES

Figure 1.1. A view of experimental setup of gyroscopic inertial sensor.....	2
Figure 1.2. Acceleration-bandwidth performance requirements of different application areas for accelerometers.	4
Figure 1.3. Dynamic model of an accelerometer.	5
Figure 1.4. Schematic of a servo type accelerometer [11].	7
Figure 1.5. Classification of magnetic bearings and magnetic levitation [12].....	8
Figure 2.1. Principle of an active magnetic bearing suspension of a rotor in vertical direction [14].	11
Figure 2.2. Magnetically linear relationship [15].	14
Figure 2.3. Forces on the rotor in magnetic bearing in one dimension.....	17
Figure 2.4. a) Block diagram of magnetic bearing system, (b) simplification of the block diagram.....	18
Figure 3.1. Electromagnetic actuator (solenoid).	23
Figure 3.2. Resistance and Inductance of each Electromagnet.	24
Figure 3.3. Ring shaped ferrite permanent magnet.	25
Figure 3.4. NdFeB ring shaped permanent magnet.....	26
Figure 3.5. The graph of radial force to radius of the rotor magnet.....	27
Figure 3.6. The figure of Unidor eddy current sensor [19].	28
Figure 3.7. Photo of the eddy current sensor in a placeholder.....	29
Figure 3.8. . Position of the eddy current sensors.	30
Figure 3.9. Eddy-current sensor spot size [20].	30
Figure 3.10. (a) TI F28377S DSP Processor LaunchPad Development Kit, (b) F28379D DSP Processor Launchpad Development Kit [22] [23].	32
Figure 3.11. Pololu MC33926 DC motor driver [25].	33
Figure 3.12. Block diagram of buffer circuit.	34

Figure 3.13. Control board of the test setup.	34
Figure 3.14. Magnetic bearing module of the test setup.....	35
Figure 3.15. CAD model of the rotor and necessary dimensions.....	36
Figure 3.16. 3D CAD model of the test setup.	37
Figure 3.17. Photo of the actual test setup.....	38
Figure 3.18. Forces and measurement axes on the rotor.	39
Figure 3.19. Active positioning (a) translational displacement; (b) inclination displacement.	40
Figure 3.20. Modeling one axis actuation in finite element analysis method program Maxwell.	42
<i>Figure 3.21. Graph of current vs radial force and linear equation.</i>	<i>43</i>
Figure 3.22. Graph of radial displacement vs radial force and linear equation.	43
Figure 3.23. Bode diagram of the plant.	44
Figure 3.24. Root locus curve of the system.	45
Figure 3.25. Design requirements line in root locus diagram.....	46
Figure 3.26. Step response and bode plot	47
Figure 3.27. Plant model of the translational displacement component.....	48
Figure 3.28. Position of the rotor under bias current.	49
Figure 3.29. Overall system model in Simulink.	50
Figure 3.30. Simulation result of translational displacement.	51
Figure 3.31. Simulink model of overall displacement model in one axis.	52
Figure 3.32. Simulation result of overall system, with translational disturbance.....	53
Figure 3.33. Simulation result of overall system, with rotational disturbance.....	53
Figure 3.34. Simulation output with different proportional constants.....	54
Figure 3.35. Simulation output with different derivative constants.	55
Figure 4.1. ADC sampling of c28 series DSP board for current feedback in Simulink.	58
Figure 4.2. PWM signal generation in C28 series DSP board in Simulink.....	58
Figure 4.3. Designed PID controller in Simulink.	59

Figure 4.4. (a) Transmitting section; (b) Receiving section of the serial communication.....	62
Figure 4.5. (a)Step response of the system; (b) noise due to Eddy current sensor. ..	63
Figure 4.6. (a) Step response of the X-axis; (b) Step response of the Y-Axis.....	65
Figure 4.7. Axis definition of STIM300 IMU.	66
Figure 4.8. Comparison with commercial sensor in x-axis.....	67
Figure 4.9. Comparison with commercial sensor in y-axis.....	68
Figure 4.10. Rotation test.....	69
Figure 4.11. Comparison with commercial sensor, maximum value.....	69
Figure 4.12. Allan Variance plot of STIM300.....	70
Figure 4.13. Random walk and Bias instability of STIM300.	71
Figure 4.14. Collected data from designed accelerometer for Allan variance calculation.	72
Figure 4.15. Allan Variance plot of designed accelerometer.....	73
Figure 4.16. Random walk and Bias instability of designed accelerometer.	73
Figure 4.17. Frequency responses.....	76
Figure 4.18. Bode plot comparison between simulation and test results.....	77

LIST OF ABBREVIATIONS

ABBREVIATIONS

IMUs	Inertial Measurement Units
AMB	Active Magnetic Bearing
CAD	Computer Aided Drawing
PD	Proportional – Derivative
PID	Proportional – Integral – Derivative
DOF	Degrees of Freedom
TI	Texas Instruments
ADC	Analog to Digital Converter
DSP	Digital Signal Processor
PWM	Pulse Width Modulation
GUI	Graphical User Interface

LIST OF SYMBOLS

SYMBOLS

m	Seismic mass
k	Spring constant
b	damping coefficient
R	Reluctance of a material
l	length of flux parth
μ	Permeability of a material
S	Cross-sectional area
g	Original air gap
x	Displacement
ψ	Flux
λ	Flux linkage
N	Turn number of winding in electromagnets
L	Inductance
i	Current
W'	Magnetic energy
W_m	Magnetic co-energy
F	Magnetic force
I_b	Bias current

i_b	Regulated current
k_i	Force-current factor
k_x	Force-position factor

CHAPTER 1

INTRODUCTION

Levitation is defined by Oxford Dictionaries as “the action of rising or causing something to rise and hover in the air, typically by means of supposed magical powers.” [1]. As a phenomenon that has captivated the human mind for centuries, levitation has not only been used by magicians to surprise their audience by creating an illusion, but also investigated by physicists to create various mechanisms of real levitation. Through these investigations, it has been discovered that there are many methods of achieving levitation, namely, aerodynamic, acoustic, optical, electrostatic, magnetic and electromagnetic [2].

1.1. Motivation

Among these different types of levitation, magnetic levitation may be widely used in many industrial applications. In their catalog, SKF points that active magnetic bearings are more suitable to turbomachinery than conventional bearings since they have wider operating range due to their precision and stability. Thanks to no friction in bearing, they do not require any oil lubrication. In this way, turbo machinery design is simplified and the need of maintenance is reduced [3].

A sensor design based on magnetic bearing implementation is also presented by Maruyama et al [4]. *Figure 1.1* shows the experimental setup of gyroscopic inertial sensor. It works as two-axis gyroscopic sensor and also three-axis servo-type accelerometer. In their study, it is mentioned that vibrating accelerometers are used in low cost applications. However, the detection sensitivity of this type of sensors is inadequate for high performance applications. On the other hand, gyroscopic sensors,

which takes benefits of active magnetic bearings, are low cost sensors for specialized works and they can measure acceleration at the same time.

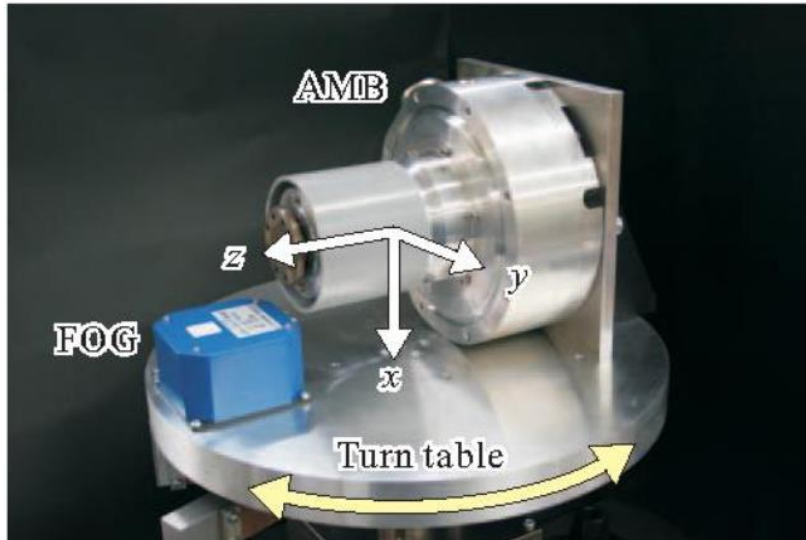


Figure 1.1. A view of experimental setup of gyroscopic inertial sensor.

It is preferred to use magnetic levitation principles especially in studies requiring high-speed applications. In a research conducted by Baumgartner, it is commented that maximum rotational speed of a reaction wheel is limited to 10 000 rpm by employed bearings. However, the researchers achieve higher speeds up to 250 000 rpm with a magnetically levitated electrical drive system [5]. Together with such an extreme speed, levitation technology allows the reaction wheels to be more compact in satellites.

Considering the benefits of levitation in engineering fields, this thesis focuses on applying magnetic levitation principles in a sensor design to measure acceleration. In a similar study, it is mentioned that magnetic levitation is a feasible technology for various industrial applications with some of the following requirements [6].

- no contact
- high precision positioning
- low vibrations

- reliability
- no contamination
- no lubrication
- high vacuum compatibility
- high speed between moving pieces

1.2. Acceleration Sensors

1.2.1. Scope of Application

Accelerometers are key sensors on measuring both static orientation and dynamic motion of an object. These devices are generally preferred for navigation applications on land, naval and air vehicles and also for robots. In addition to that, they are used for sensing the shock or vibration on an object. For example, different types of accelerometers aim to detect seismic motion on ground or free fall of a hard drive to be able to protect it. Furthermore, inertial measurement units (IMUs) have inertial sensors such as gyroscopes and accelerometers. They help tracking the position of an object or stabilizing a platform. Figure 1.2 shows the application areas of accelerometers and required resolution versus bandwidth performances [7].

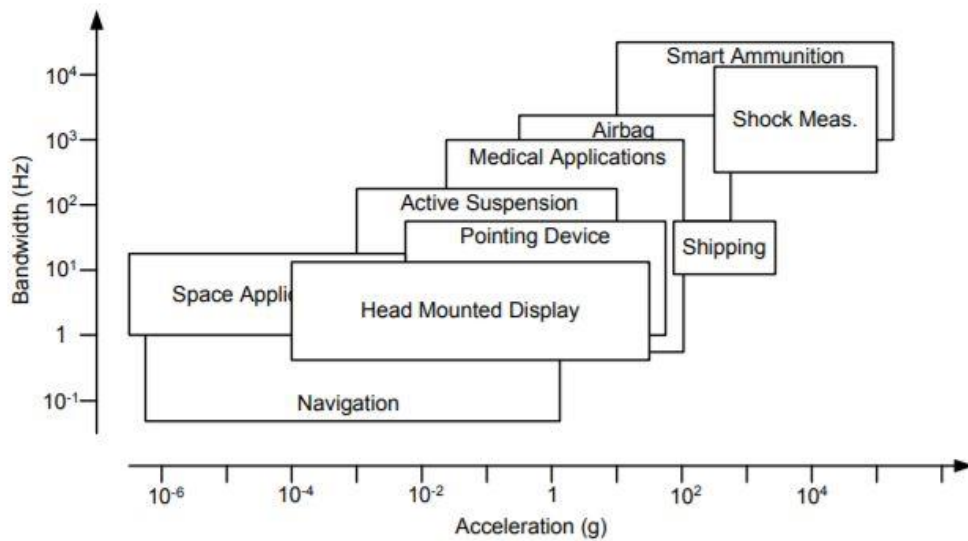


Figure 1.2. Acceleration-bandwidth performance requirements of different application areas for accelerometers.

1.2.2. Basic Operational Principle

There are several accelerometer types depending on their measurement methods. Working principles of accelerometers are based on Newton's second law of motion, which could be stated as follows: "any object undergoing acceleration is responding to a force". In general, the operation of an accelerometer can be modeled as mass spring damper system[8] as seen in Figure 1.3.

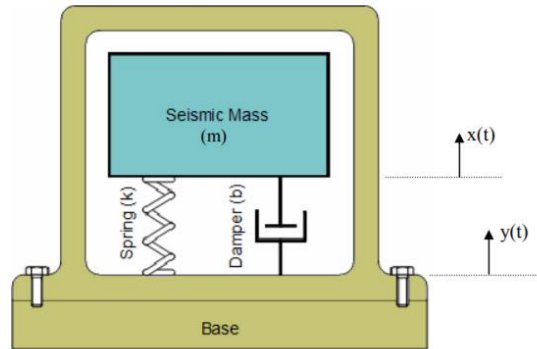


Figure 1.3. Dynamic model of an accelerometer.

A seismic mass as m is connected to a supporting base by a spring and there is also a damper for energy loss, where k is the spring constant and b is the damping coefficient. It is known that the equation of such system is shown below [9].

$$m\ddot{z}(t) + b\dot{z}(t) + kz(t) = -ma(t) \quad (1.1)$$

Where

$$z(t) = x(t) - y(t) \quad (1.2)$$

And

$$a(t) = \ddot{y}(t) \quad (1.3)$$

It should be noted that there is a minus sign in front of the term representing force applied by the external acceleration. This indicates that the displacement of the seismic mass is in the opposite direction with the applied acceleration.

1.2.3. Types of Accelerometers

As mentioned previously, the types of accelerometers vary according to their working principles. For example, piezoresistive accelerometers detect the deflection of a beam under some action by changing the resistance itself. Capacitive accelerometers measure the difference in capacitance in between two parallel planes, one is stationary

and the other plate is moving with the exerted acceleration. On the other hand, most commonly used accelerometers are electromechanical types, which are also known as servo type accelerometer. Comparison of the types of the accelerometers can be made and tabulated as in Table 1.1 [10].

Table 1.1. Comparison of accelerometer types [10].

Accelerometer Type	Advantages	Limitations	Typical Applications
Piezoresistive Accelerometer	<ul style="list-style-type: none"> • DC response • Small Size 	<ul style="list-style-type: none"> • Lower Shock Protection • Smaller Dynamic Range 	<ul style="list-style-type: none"> • Crash Testing • Flight Testing • Shock Testing
Capacitive Accelerometer	<ul style="list-style-type: none"> • DC Response • Better Resolution than PR Type 	<ul style="list-style-type: none"> • Frequency Range • Average Resolution 	<ul style="list-style-type: none"> • Ride Quality • Ride Simulation • Bridge Testing • Flutter • Airbag Sensor • Alarms
Servo Accelerometer	<ul style="list-style-type: none"> • High Sensitivity • Highest Accuracy for Low Level Frequency Measurements 	<ul style="list-style-type: none"> • Limited Frequency Range • High Cost • Fragile, Low Shock Protection 	<ul style="list-style-type: none"> • Guidance Applications Requiring Little or no DC Baseline Drift

Figure 1.4 shows the concept of a servo type accelerometer, which is also called as force balance accelerometer. The working principle of the servo type accelerometers is built on sensing the motion by a displacement detector and feeding the proper amount of current to the coil in order to return the proof mass to its original position. This current will be proportional to the acceleration, which is converted to an output voltage [11].

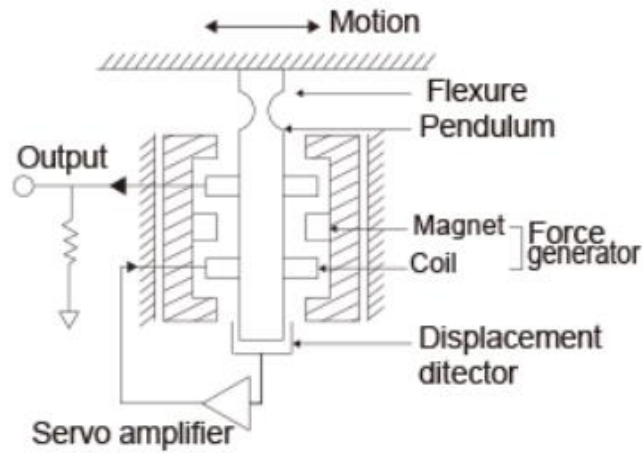


Figure 1.4. Schematic of a servo type accelerometer [11].

1.3. Magnetic Levitation

Despite their high performance and reliability, building an Inertial Measurement Units needs both coriolis accelerometers (rate gyroscopes) and linear accelerometers. Since rotary rate gyroscopes have superior performance specifications compared to vibratory rate gyroscopes, developing a levitated linear accelerometer enables development of levitated rotary rate gyroscopes. In order to achieve magnetic levitation, magnetic bearings are introduced in servo type accelerometer design.

Magnetic bearings consisting of permanent magnets and electromagnets eliminate the mechanical contact problem. Active magnetic actuation is applied not only for levitation but also for position control of the proof mass. Because the magnetic bearings eliminate mechanical contact, neither wear nor limited life problems exist. This kind of magnetic levitation allows the accelerometer to obtain more than single axis linear acceleration information. In the magnetically levitated accelerometer design, two axes angular and two axes linear acceleration information can be gathered.

In addition to that, as the mechanical contact is prevented, low wear, low operation life and high linearity are obtained and assessed at the end of this study.

Existing magnetic levitation techniques can be categorized and presented as an overview diagram as seen in Figure 1.5. Calculation of magnetic force from energy is relatively a simpler method rather than that of Lorentz-Force method. It is shown in Figure 1.5 that only low forces can be generated via diamagnetic materials. Moreover, superconductors, which are based on Meissner-Ochsenfeld effect, are not compatible with an inertial sensor design because they need extremely low temperatures. Achieving and maintaining such low temperature values require enormous power consumption [12]. Therefore, the use of classical active magnetic bearings seems to be best and only choice to design an acceleration sensor in this study.

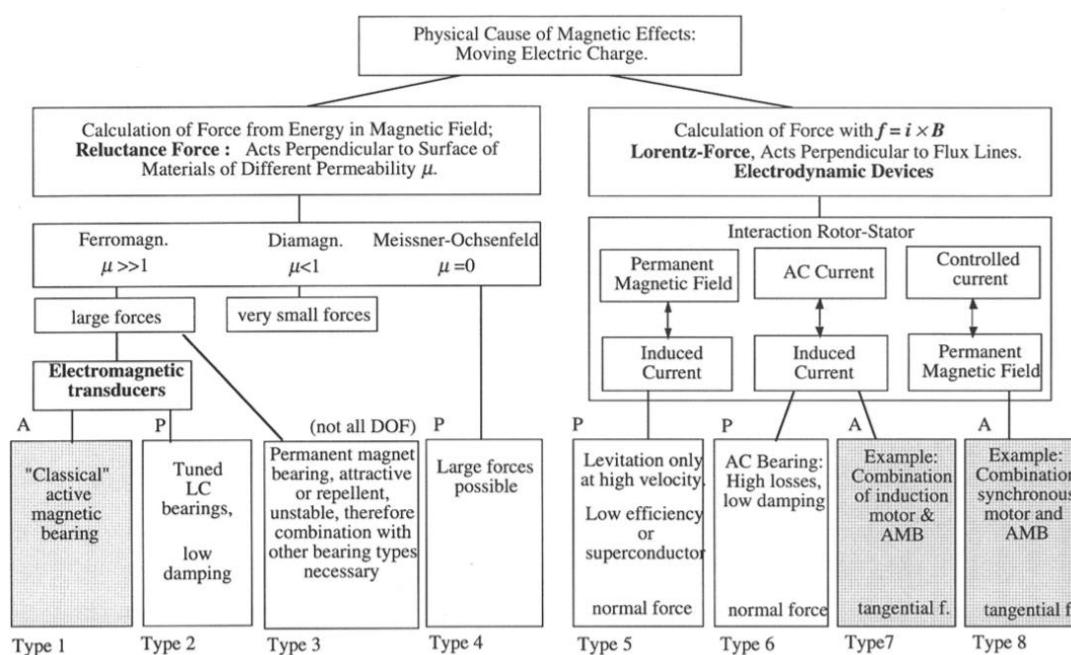


Figure 1.5. Classification of magnetic bearings and magnetic levitation [12].

As also shown in Figure 1.5, the combination of motor and active magnetic bearings is another application of magnetic bearings. These fields of application involve the studies on designing bearingless motors or contactless gyroscopes, which will be

mentioned in the last chapter as future works. Yet, the scope of this thesis is limited to classical active magnetic bearing and its usage in an acceleration sensor.

1.4. Thesis Organization

As explained in the first chapter, active magnetic bearing technology comes with various benefits. Using this technology in a sensor design is motivating since it enhances the measurement performance and lifetime of the accelerometer. Furthermore, the cost and size of the sensor can be reduced by this method. In this chapter, some examples are given to describe how important a contactless sensor technology is. Accelerometers are compared not only for different application areas but also for their sense technologies. Basic working principle of an accelerometer and magnetic bearing system for levitation are briefly introduced.

In the second chapter, theoretical background of the magnetic bearing technology is given in detail. The equations for magnetic force calculation is derived. At the end of this chapter, stabilization characteristics of magnetic bearings are discussed and a suitable controller selection is made.

In the third chapter, test setup for accelerometer measurement is shown with detailed figures. The components of setup and their specifications are explained. 3D CAD model is drawn in Solidworks 2016 to collect some information such as air gap lengths, mass of the rotor and rotor inertia values etc. Besides, magnetic force analysis is accomplished by the computer program, ANSYS Maxwell, which uses finite element methods for different current and displacement values. After all, a dynamical model is built to perform some simulations in MATLAB/Simulink environment. A PID controller is added to the simulations and performance of the system is shown with graphs. Besides the settling time and bandwidth of the system, measurement limits are also calculated and simulated in this chapter.

In the fourth chapter, tests are conducted to investigate the performance of the test setup. The results of these tests are shared in this chapter. The limits of the test setup is discussed based on the test results. A comparison of the designed accelerometer with a commercial inertial measurement unit is shown at the end of this chapter.

In the last chapter, magnetic levitation technology, its benefits to accelerometer design and lastly the design process of the setup is summarized. Conclusions reached are presented and some possible research points for future studies are discussed.

CHAPTER 2

ACTIVE MAGNETIC BEARING

As quoted by Maxwell, Earnshaw's theorem states that: "A charged body placed in a field of electric force cannot be in stable equilibrium." [13]. In other words, this theorem proves that the suspension of objects with electrostatic and magnetic fields is not possible. This does not mean that magnetic levitation is impossible. In order to achieve levitation, some engineering is needed such as use of active magnetic components and feedback control of position of the levitated object.

Before elaborating on magnetically levitated accelerometer design, active magnetic bearings should be discussed since the concept of active magnetic bearing is the key factor for levitation and contactless drive. *Figure 2.1* presents the main components and explains the function of a simple bearing for suspending a rotor only in one direction [14].

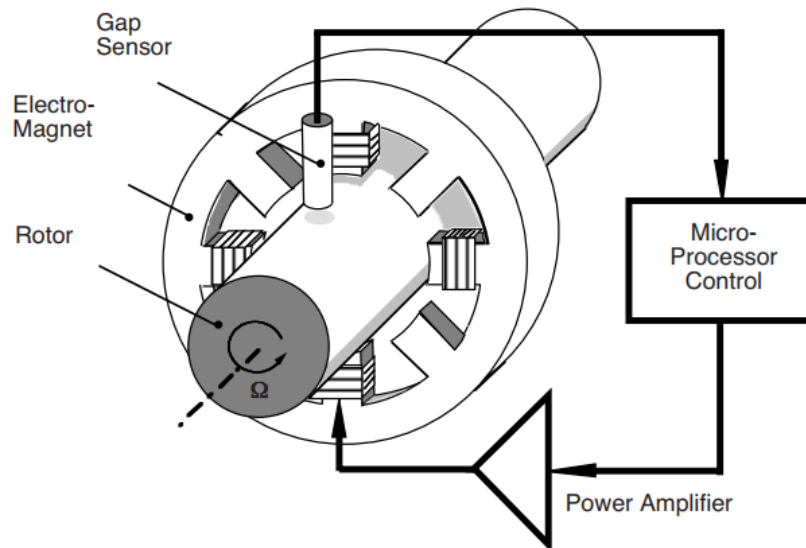


Figure 2.1. Principle of an active magnetic bearing suspension of a rotor in vertical direction [14].

A contactless position sensor, which is most often selected from an eddy current, capacitive or an inductive type, is used to measure the gap between rotor and electromagnet. Microprocessor drives control algorithm to calculate the necessary amount of current from the error between reference position and sensor measurement. The primary goal of the controller is not only to maintain the rotor position at a desired value but also to achieve the stabilization of the overall control loop. Power amplifier converts the control signal to electric current feeding into coils of the electromagnets and creates magnetic field in the iron of the electromagnet. The combination of power amplifier and bearing electromagnet is also called the electromagnetic actuator in the literature [14]. Thus, desired magnetic force is generated at the end of the process. The analysis of the magnetic bearings is investigated in the next chapter.

2.1. Analysis of Magnetic Bearing

Considering one pole of the magnetic bearing in Figure 1.3 with the assumption of linear system, equations are derived in this chapter. Reluctance of a material in the magnetic circuit is calculated as follow.

$$R = \frac{l}{\mu S} \quad (2.1)$$

Where l is the length of the flux path, μ is the permeability of the material and S is the cross sectional area. The flux path varies with the position of the rotor. g is taken as the original gap and x is taken as position difference of the rotor.

$$R = \frac{g - x}{\mu S} \quad (2.2)$$

There are rotor, stator and air with different types of materials in a magnetic circuit. However, air has a relative permeability as approximately 1.0. So, the reluctance of air is significantly larger than that of the other materials. For example, the relative

permeability of the iron in rotor or in electromagnet is typically in the range of 1000 – 10 000. Therefore, magnetic circuit can be simplified. The flux is then,

$$\psi = \frac{Ni}{R_{air}} = \frac{Ni\mu S}{g - x} \quad (2.3)$$

The flux linkage, λ , in the electromagnet is defined as flux multiplied by number of turns N .

$$\lambda = \frac{N^2 i \mu S}{g - x} \quad (2.4)$$

Inductance, L , is the flux linkage divided by the current, i , passing through windings.

$$L = \frac{N^2 \mu S}{g - x} \quad (2.5)$$

Displacement of the rotor, x , is quite small compared to air gap, g . Therefore, only first and second terms of the series expansion form of eq. 2.5 can be examined as follow.

$$\frac{1}{g - x} = \frac{1}{g} \frac{1}{\left(1 - \frac{x}{g}\right)} = \frac{1}{g} \left(1 + \frac{x}{g} + \frac{x^2}{g^2} + \frac{x^3}{g^3} + \dots\right) \quad (2.6)$$

$$L = L_0 \left(1 + \frac{x}{g}\right) \text{ where } L_0 = \frac{N^2 \mu S}{g} \quad (2.7)$$

The magnetic energy, W' , stored in the system and magnetic co-energy, W'_m is equal if the magnetizing characteristic curve is assumed to be linear [15] as in *Figure 2.2*.

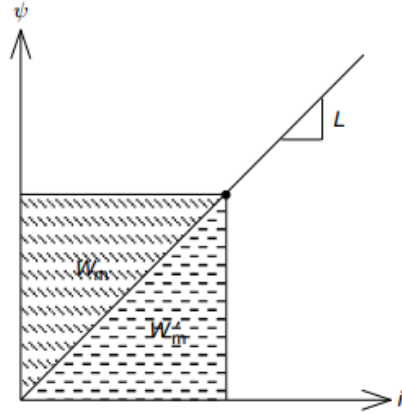


Figure 2.2. Magnetically linear relationship [15].

This linearity yields the following simple energy equation.

$$W_m' = \int_0^i L i di = \frac{1}{2} L i^2 \quad (2.8)$$

Thus, the magnetic force F is written as follows by figuring out that $\frac{\partial L}{\partial x}$ is equal to $\frac{L_0}{g}$.

$$F = \frac{\partial W_m}{\partial x} = \frac{\partial L}{\partial x} \frac{i^2}{2} = \frac{L_0}{g} \frac{i^2}{2} = k_i' i^2 \quad (2.9)$$

Equation (2.9) shows that magnetic force is proportional to square of the current, which is a nonlinear relationship. However, in practice, it could be assumed that the magnetic force is proportional to the current, as Chiba states in his book “Magnetic Bearings and Bearingless Drive” [15]. In order to realize the linearity, current in the electromagnet is separated into two parts as the bias current, I_b , and regulated current, i_b .

$$i = I_b + i_b \quad (2.10)$$

It can be considered that regulated current should be less than the bias current to linearize the equation. Hence, the following simplified force equation can be obtained.

$$F = k_i' I_b i_b = k_i i_b \quad (2.11)$$

Where k_i is referred to as a force current factor [16]. It is seen that the radial force is proportional to the force regulating current when the bias current is kept constant. Because of this relation, instantaneous current could be controlled in most cases. Current sensors are cheap and most often it is included in drivers. Moreover, measuring current is easier than measuring flux for force calculation. Current controller is also recommended by A. Chiba due to these aforementioned reasons [15].

2.2. Stabilization Analysis of Active Magnetic Bearings

Previous derivations show the relation between magnetic force and current passing through electromagnets by assuming that the change in position of the rotor is much smaller than air gap. However, the change in the distance between rotor and stator should also be considered when the air gap is decreased remarkably to get higher force capability in active magnetic bearing design.

2.2.1. Unstable Force Component

If the air gap starts to decrease due to movement of the rotor, the magnetic force will increase rapidly. This aspect causes an unstable force mechanism in the bearing system. The unstable pull force is a function of the eccentricity. This can perform as an inherently negative spring mechanism. In order to achieve a successful magnetic bearing system, negative feedback force should be applied to cancel this unstable pull force.

The principles of unstable force points out that magnetic force is not only a function of current but also a function of displacement [15]. In Equation (2.7), an approximation is used and only first two terms is examined in derivations. However, unstable force arises due to the third and higher terms. The third term should be appended in equations to consider unstable force effect as follow.

$$L = L_0 \left(1 + \frac{x}{g} + \frac{x^2}{g^2} \right) \quad (2.12)$$

Then, magnetic force energy equation becomes following.

$$W = \frac{1}{2} i^2 L_0 \left(1 + \frac{x}{g} + \frac{x^2}{g^2} \right) \quad (2.13)$$

Thus, magnetic force is obtained by taking partial derivative of magnetic energy.

$$F = \frac{L_0}{2g} i^2 + \frac{L_0}{g^2} i^2 x \quad (2.14)$$

$$F = k_i' i^2 + k_x x \quad (2.15)$$

It can be seen clearly from Equation (2.15), magnetic force is not only a function of current but also that of position. Moreover, the second term corresponds to unstable component of the force. In a similar way to mention k_i previously, k_x is called as force position factor of magnetic bearings. By considering winding current is approximately equal to bias current, I_b , as in the Equation (2.11) then force factors are as follows.

$$F = k_i i + k_x x \quad (2.16)$$

$$k_i = \frac{L_0}{2g} I_b \quad (2.17)$$

$$k_x = L_0 \left(\frac{I_b}{g} \right)^2 \quad (2.18)$$

After concentrating on magnetic force, now force balance by considering the mass of the rotor should be focused on. Figure 2.3 shows the free body diagram of the rotor in the magnetic bearing system.

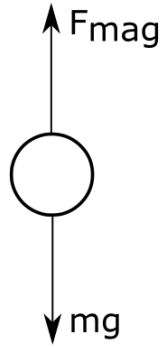


Figure 2.3. Forces on the rotor in magnetic bearing in one dimension.

The only force on rotor is gravitational force, mg , and magnetic force F_{mag} . The total force relation is then,

$$ma = F_{mag} - mg \quad (2.19)$$

$$m(a + g) = ma' = F_{mag} \quad (2.20)$$

$$m\ddot{x} = k_i i + k_x x \quad (2.21)$$

This equation is a good way to obtain a transfer function and draw the block diagram of the open loop system. In order to get a transfer function, first it is needed to be take the Laplace Transform of above equation.

$$ms^2X(s) = k_i I(s) + k_x X(s) \quad (2.22)$$

$$\frac{X(s)}{I(s)} = \frac{k_i}{ms^2 - k_x} \quad (2.23)$$

After this transformation, the block diagram which is illustrated in Figure 2.4, is generated from the transfer function.

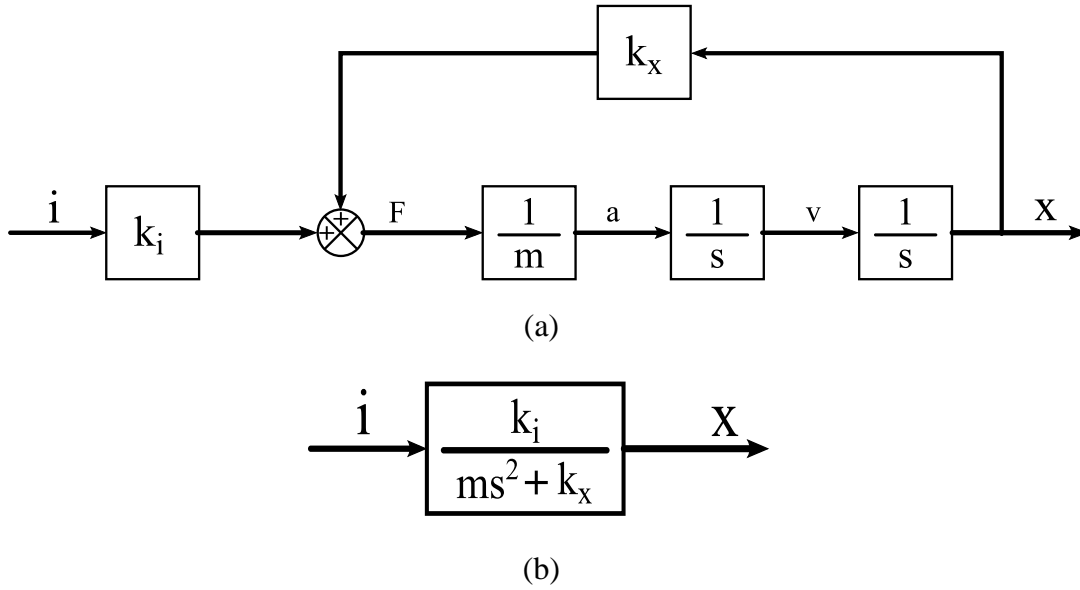


Figure 2.4. a) Block diagram of magnetic bearing system, (b) simplification of the block diagram.

As seen in the block diagram, the component of magnetic force related to displacement adds a positive feedback inherently. That makes the transfer function unstable. Therefore, the system requires negative feedback to cancel the effect of this component. Furthermore, the roots of the characteristic equation is in the following.

$$s_{1,2} = \pm \sqrt{\frac{k_x}{m}} \quad (2.24)$$

One of the poles of the plant is in the right half plane. By looking at this positive root, it can be stated that the magnetic bearing system is unstable unless a feedback controller is added.

2.2.2. State Space Representation

State space description of active magnetic bearing systems are quite useful to include non-mechanical quantities such as the coil voltage and flux in the system. Moreover,

treating the system in state space representation makes it possible to address some non-measured states such as rotor velocity.

The interpretation of system states can be done variously for each dynamic system, thus, different state space descriptions can exist yet yielding the same dynamic properties. There is a simple relationship between the order of the state space representation and the number of mechanical degrees of freedom (DOF). As a mechanical system features, two “storage units” for each DOF, i.e. kinetic and potential energy, two state variables, mostly position and velocity, must be attributed to each DOF. Therefore, state space representation of a simple one DOF magnetic bearing system can be developed with two state variables chosen as position and velocity of the rotor. Then, the state vector in the follow is selected.

$$x = \begin{bmatrix} x \\ v \end{bmatrix} \quad (2.25)$$

The derivative of the velocity, which is acceleration, can be gathered from the force relation.

$$\dot{v} = \frac{k_i}{m} i + \frac{k_x}{m} x \quad (2.26)$$

After introducing the current, i , as an input; a well-known state space description is obtained from the combination of Equation (2.25) and Equation (2.26).

$$\dot{x} = Ax + Bu \quad (2.27)$$

$$A = \begin{bmatrix} 0 & 1 \\ \frac{k_x}{m} & 0 \end{bmatrix}, B = \begin{bmatrix} 0 \\ \frac{k_i}{m} \end{bmatrix}$$

Note that the coil current is the only element of input. Furthermore, the eigenvalues of the matrix are $\lambda_{1,2} = \pm \sqrt{\frac{k_x}{m}}$. That is also the same result with the Equation (2.24).

2.3. Controller Selection

A simple controller suitable for magnetic levitation applications is a PD controller. Following chapter focuses on the controller of the magnetic bearing system. First, general transfer function of PD controller is written as follow.

$$G_C = K_P + sT_D \quad (2.28)$$

Where K_P is the proportional gain constant and T_D time constant of the derivative portion. Open loop transfer function is then as follows.

$$G_{OL} = (K_P + sT_D) \left(\frac{k_i}{ms^2 - k_x} \right) \quad (2.29)$$

After the multiplication of plant with the controller, characteristic equation is gathered by equating denominator to zero. Solving the characteristic equation gives new poles of the overall system.

$$ms^2 + k_iT_Ds + (k_iK_P - k_x) = 0 \quad (2.30)$$

$$s = \frac{1}{2m} \left[-T_Dk_i \pm \sqrt{(T_Dk_i)^2 - 4m(k_iK_P - k_x)} \right] \quad (2.31)$$

This equation, which gives the poles of the system, provides some conditions in order to ensure the stability of magnetic suspension.

(a) If T_D is zero and $K_P = 0$ then the value of the roots are

$$s = \frac{1}{2m} \left[\pm \sqrt{4m(k_x)} \right] \quad (2.32)$$

That is the same as previous derivations giving one positive pole, which means instability.

(b) If T_D is zero and $K_Pk_i - k_x > 0$ then the value inside the bracket is

$$[\] = \pm j\sqrt{4m(K_p k_i - k_x)} \quad (2.33)$$

That means there are two poles located on the imaginary axes. It corresponds to marginal stability that is not useful in practice.

(c) If T_D is positive and $K_p k_i - k_x > 0$ then

$$[\] = -T_D k_i \pm j\sqrt{(T_D k_i)^2 - 4m(K_p k_i - k_x)} \quad (2.34)$$

Hence, both poles are located in the left half plane, which gives the stability for feedback system.

Therefore, derivative action is an obligation for magnetic suspension of feedback loop stability.

At this point, an examination on the usage of integration action for a controller in magnetic suspension systems is required also. The reference for displacement is set to be zero in general for magnetic levitation systems. The gap between rotor and electromagnet is being increased with only a PD controller. This is due to the steady state error occurring when an external static force is applied. In many applications, integrator factor is put to the controller also in order to compensate this error. Therefore, the PID controller is preferred in this thesis to design a magnetically levitated accelerometer.

CHAPTER 3

EXPERIMENTAL SETUP

The main purpose of this thesis is to design a sensing mechanism using a levitated proof mass. In this chapter, the material selection and the component of the system are discussed in detail. This includes feedback devices, electronic circuits and microprocessor besides magnetic elements in the system.

In design process of experimental setup, low cost materials are chosen. First, the module for levitation is built with permanent magnets and also electromagnets and then, the sensors are placed around the rotor. After that, the electrical circuits and control algorithms are implemented to the system.

3.1. Components of the Setup

3.1.1. Electromagnetic Actuators

The actuators shown in *Figure 3.1* are preferred because they can be readily purchased for levitation applications of small loads.

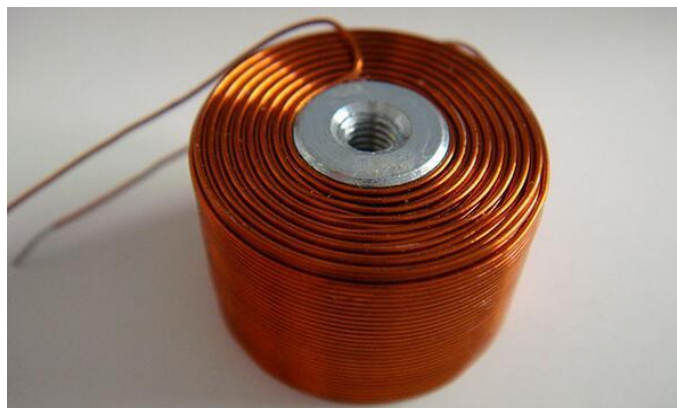


Figure 3.1. Electromagnetic actuator (solenoid).

There are four solenoids in one module of the system, two for each axis. There are also two modules for bottom and upper part of the structure. That means that the setup has eight electromagnetic actuators in total. The outer diameter of the steel core, which is in the center of the copper winding, is 8mm and its height is 12 mm. The core has a M3 threaded hole to ease mounting.

The enameled copper wire, which has a size AWG 28, is wounded 450 turns around electro magnet core. Individual direct current resistance of each actuator is measured as 3.74Ω and inductance value is measured to be around 3.56mHenry. The measurement is done by a LCR meter as shown in Figure 3.2

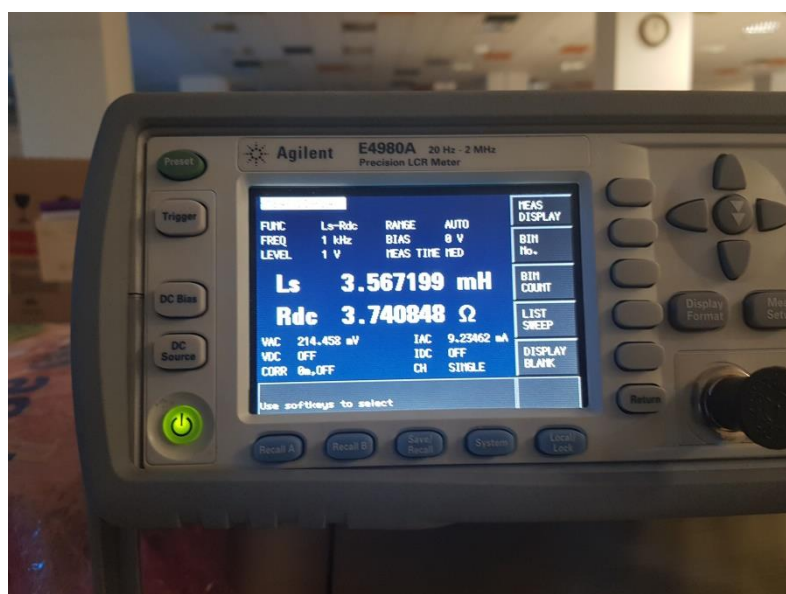


Figure 3.2. Resistance and Inductance of each Electromagnet.

The distance between electromagnets is 38 mm from center to center. If electromagnets are placed closer, then the coupling affects become remarkable in between magnetic fields of the electromagnets.

3.1.2. Permanent Magnets

3.1.2.1. Ferrite Permanent Magnets

Ring shaped permanent magnets are used in both stator and rotor to be able to create forces not only in axial direction but also in radial direction. On the stator side, ring shaped ferrite permanent magnets, as shown in *Figure 3.3*, with 100mm outer and 60mm inner diameter and 10mm height are used to create axial force. These magnets are magnetized in the axial direction along their symmetry axis, which is also show in *Figure 3.3*. There are totally two ferrite magnets on the test setup, each is placed stator of active magnetic bearing placed with same magnetic poles facing each other to create repulsive forces on the rotor. The reason why repulsive forces are created on the rotor is to ensure stability. If attractive forces would be preferred, then with decreasing gap between the rotor and stator, the forces would also increase and permanent magnets stick together due to unstable characteristics of the repulse forces on permanent magnets.

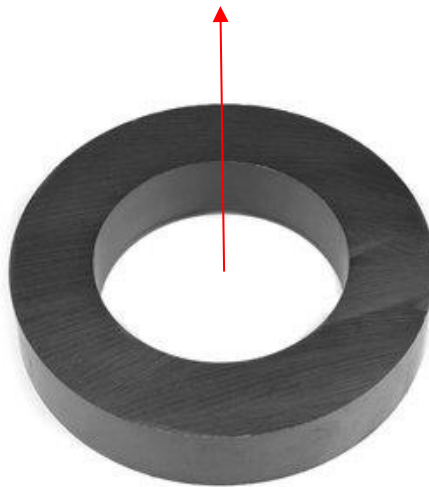


Figure 3.3. Ring shaped ferrite permanent magnet.

Ferrite magnets are preferred for the stator side because of their high availability and lower prices. The ferrite materials are Ceramic C8 and its physical characteristics are given in *Table 3.1*. Here B_r is the remanent magnetic flux density, H_c is the normal

coercivity, H_{ci} is the intrinsic coercivity and BH_{max} is the maximum energy product of the permanent magnet.[17]

Table 3.1. Characteristics of C8 ferrite permanent magnet [17]

Material	Br [mT]	Hc [kA/m]	Hci [kA/m]	BHmax [kJ/m ³]
C8	385	235	242	27,80

3.1.2.2. Neodymium Magnets

On the rotor side, smaller permanent magnets with higher energy density are preferred in order to keep rotor small and lightweight. Because of that reason, NdFeB type permanent magnets, which has 25mm outer diameter and 6mm inner diameter with 10mm height, are preferred as rotor magnets as shown in *Figure 3.4*. These magnets are also magnetized in the axial direction along their symmetry axis, which is show in *Figure 3.4*.



Figure 3.4. NdFeB ring shaped permanent magnet.

The NdFeB magnet type is stated as N45 and its physical characteristics are given in the *Table 3.2*. Here the explanation of the characteristics are the same as the ones explained in the ferrite magnet as well [18].

Table 3.2. Characteristic of N45 neodymium permanent magnet [18].

Material	Br [mT]	Hc [kA/m]	Hci [kA/m]	BHmax [kJ/m ³]
N45	1350	876	955	354

In the magnetic analysis of electromagnets and permanent magnet on the rotor, it is figured out that there is saturation in radial force even the diameter of rotor magnet is getting larger. The analysis result is shown in *Figure 3.5*.

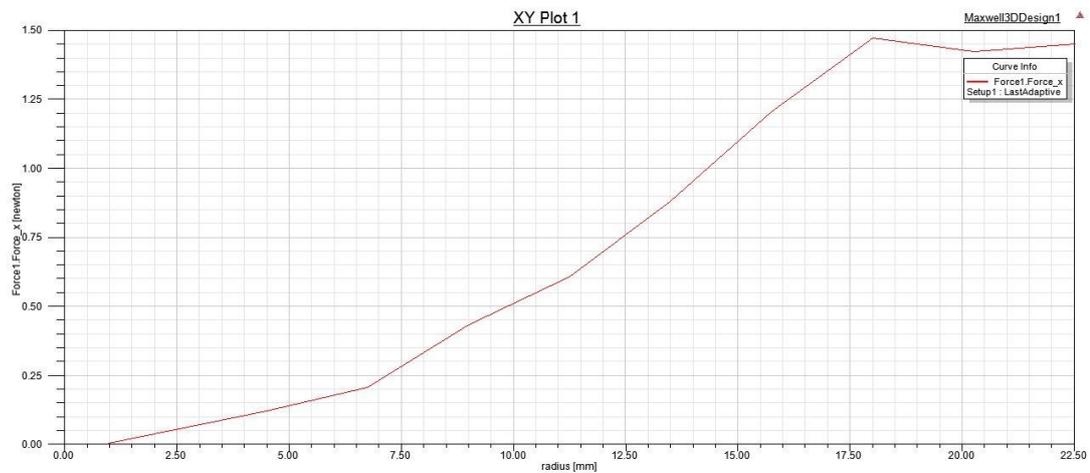


Figure 3.5. The graph of radial force to radius of the rotor magnet.

Analysis result shows that the diameter of the rotor magnet bigger than 17.5 mm is affectless on the radial force. This is because the magnetic field is generated between rotor and electro magnet core produces the radial force. The force varies with the area of electromagnets core facing with rotor magnet. After some point, the area does not differ so much which means that effect on the force can be neglected. Therefore, small magnets can be used for this setup by considering the weight of the rotor.

3.1.3. Position Sensors

The position of the rotor must be measured to be able to control active magnetic bearings. There are various types of sensors to feedback the position. Among them,

capacitive and eddy current types are the ones that are more precise. Capacitive ones have a disadvantage that they demand external circuitry for signal conditioning. On the other hand, eddy current sensors are more useful for this type of an application because they are smaller in size and have simpler structure. Because of their advantages including high measurement bandwidth, eddy current sensors are used to measure rotor position in the radial directions of the setup. The chosen sensor is WSD S2/10M-F from Unidor [19] and it can be shown in Figure 3.6. This particular sensor has 2mm measuring range and has a resolution of $1.5\mu\text{m}$ for static and $5\mu\text{m}$ for dynamic measurements. The WSD S2/10M-F has analog output in the range 0 – 13 Volts. Sensor output is decreasing linearly when a metal conducting surface comes close to sensor.

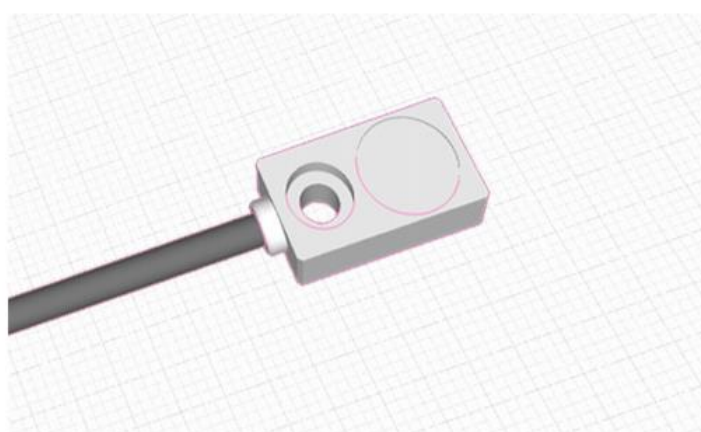


Figure 3.6. The figure of Unidor eddy current sensor [19].

The selected sensor has also a hole to assemble it with m3 bolt. The photo of the eddy current sensor can be seen in its holder, in Figure 3.7. For both upper and bottom side of the magnetic bearings, two of these sensors are used to measure position difference in orthogonal directions as seen in Figure 3.8. It means that four sensors in total are used to measure radial position of the rotor. Moreover, one additional sensor should also be used to measure rotor position for axial direction.

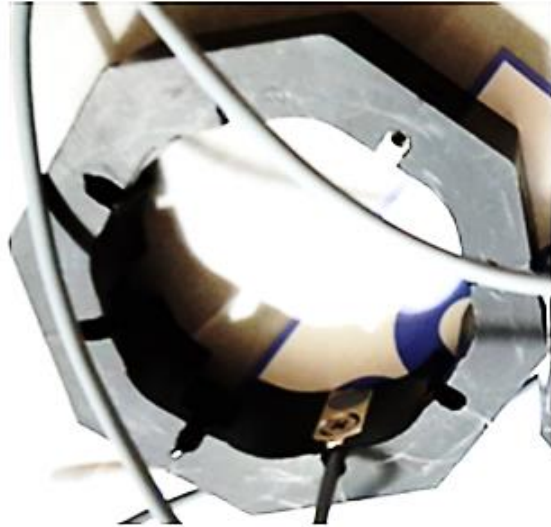


Figure 3.7. Photo of the eddy current sensor in a placeholder.

As shown in Figure 3.8, the eddy current sensors, colored in red, are measuring the position of the aluminum sensor target rings, not the position of the rotor magnets. It should be noted that the output characteristic of sensor is different when the material in front of it changes. In this setup, an aluminum target is manufactured to assemble the rotor, which is positioned exactly in front of the sensor.

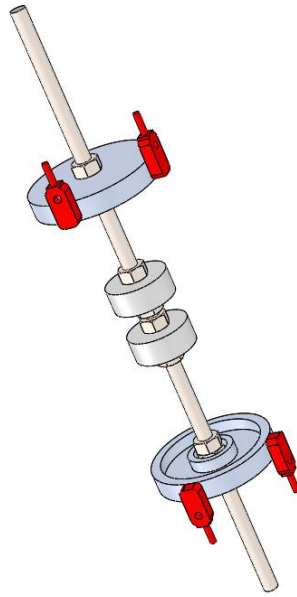


Figure 3.8. . Position of the eddy current sensors.

Eddy-current sensors use magnetic field in such a way that they completely surround the end of the probe. Thus, comparatively large sensing field is generated in a spot size approximately three times the probe's sensing coil diameter [20], as seen in Figure 3.9.

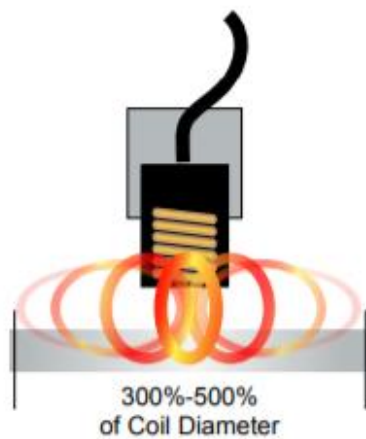


Figure 3.9. Eddy-current sensor spot size [20].

Therefore, it is important that the thickness of the sensor target should not be less than probe's sensing coil diameter for using eddy current sensors. Because of this reason, thickness of the sensor target is enlarged to two times of sensing diameter of the selected sensor. By increasing the thickness, weight of the rotor is increased too, which is an unwanted result. Therefore, the shape of the sensor target is specialized to decrease weight.

3.1.4. Processor

In order to implement real time controller, an evaluation board of Texas Instruments (TI) with F28377S Delfino Digital Signal Processor (DSP) is selected [21]. Development Kit, as seen in *Figure 3.10 (a)*, of this processor has enough and adequate digital and analog interfaces and promoted by the TI to be used in real time control applications similar to this study. The built-in interfaces of the development kit are CLA, 1 MB Flash, 16-bit/12-bit ADCs, comparators, 12-bit DACs, delta-sigma sync filters, HRPWMs, eCAPs, eQEPs, CAN and the F28377s processor has 200MHz clock with enough computing power [22].

The main advantage of using TI's C2000 Processors is the code generation tool chain with Matlab/Simulink environment. Simulink has built in libraries and blocks allowing easy configuring and access to processor's peripherals.

During experimenting with the ADC(Analog/Digital Converter) of the Launchpad, it is observed that there is a design error on the ADC module such that, sampling frequency and quantization errors observed on the digitized signal. Official release of the F28377s Launchpad also stated the same problem, so that TI made the F28377s board obsolete.

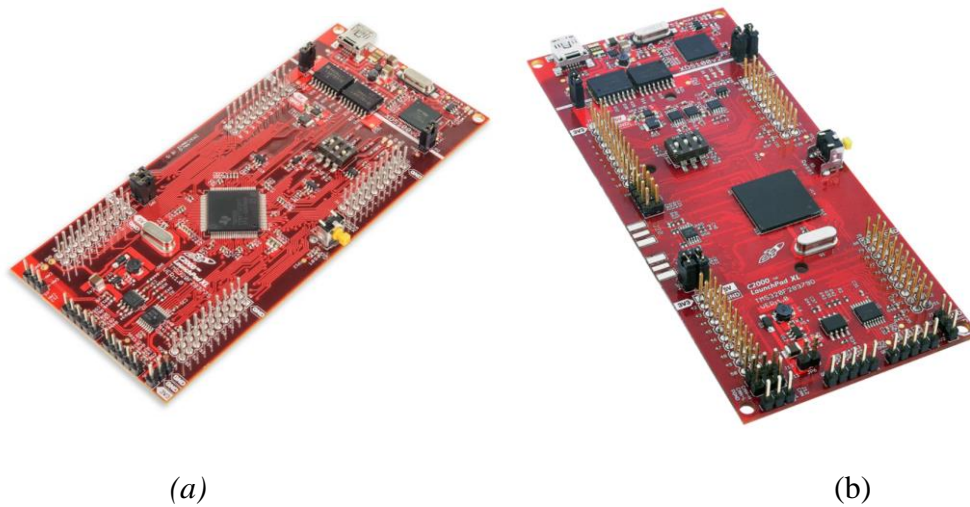


Figure 3.10. (a) TI F28377S DSP Processor LaunchPad Development Kit, (b) F28379D DSP Processor Launchpad Development Kit [22] [23].

In order to replace erroneous development board, TI's new F28379D Launchpad Development kit [23] with dual core processor is changed with the F28377S board. With the new development board, shown in *Figure 3.10 (b)*. ADC sampling problem is solved and controller implementation is continued with the new board.

On this evaluation boards, there is a built-in FTDI serial communication chip, allowing easy access to board via USB communication protocol as well. The FTDI chip is also connected to processor via SCI protocol [24].

3.1.5. Power Amplifier

In order to energize the electromagnets in a controlled way, appropriate switching circuitry is required. In order to pass current in both directions, a full H bridge circuitry is desired. Rather than designing the whole bridge from the beginning, first a readily available L298N motor driver circuitry is used. This integrated circuit is capable of providing 1.5Amps continuously and 2Amps with a restricted duty cycle. At the beginning working at 12Volts, the L298N driver IC was capable of delivering enough current however, in order to increase forces created on the bearing, the working

voltage is increased to 24Volts and at that voltage the current is doubled too. As L298N could not handle the increased current, at the final design Pololu MC33926 Motor Driver, shown in *Figure 3.11*, with 3.5Ampers continuous and 5 Ampers peak current is replaced with the old L298N driver IC. Switching to MC33926 Motor Driver also brought the advantage of obtaining current feedback with 0.525 Volt/Ampers scaled outputs [25].



Figure 3.11. Pololu MC33926 DC motor driver [25].

3.1.6. Buffer IC

As F28379D is a 3.3Volt compatible processor, the ADC of the processor is also capable of converting analog signals up to 3.3Volt. The eddy current sensors give output in the range of 0 -13Volts so that, an outer dividing circuitry is required. In order to divide a sensor output, a division with resistors is sufficient if the sensor output has enough impedance. In the case of Unidor WSD S2/10M-F, the output impedance is not high enough. In order to divide the sensor output without degrading its impedance, a non-inverting buffer circuitry is utilized with LF347N operational amplifier. Although this operational amplifier has four channels, two channels are used for each operational amplifier. In total two operational amplifiers are used for

both active magnetic bearings. In order to prepare Unidor WSD S2/10M-F eddy current sensor output for A/D conversion at F28379D processor, buffered signal output is divided by five with the corresponding resistor values shown in *Figure 3.12*.

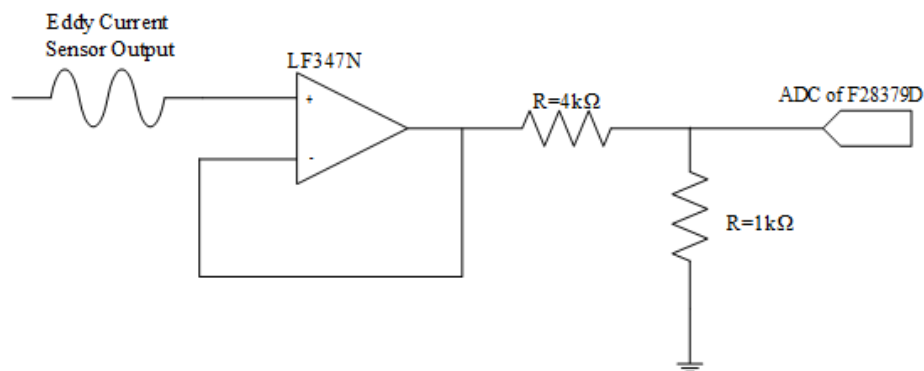


Figure 3.12. Block diagram of buffer circuit.

The buffer chips and amplifiers with voltage regulators and connector are soldered to a circuit board shown in *Figure 3.13*, such that whole components packed together.

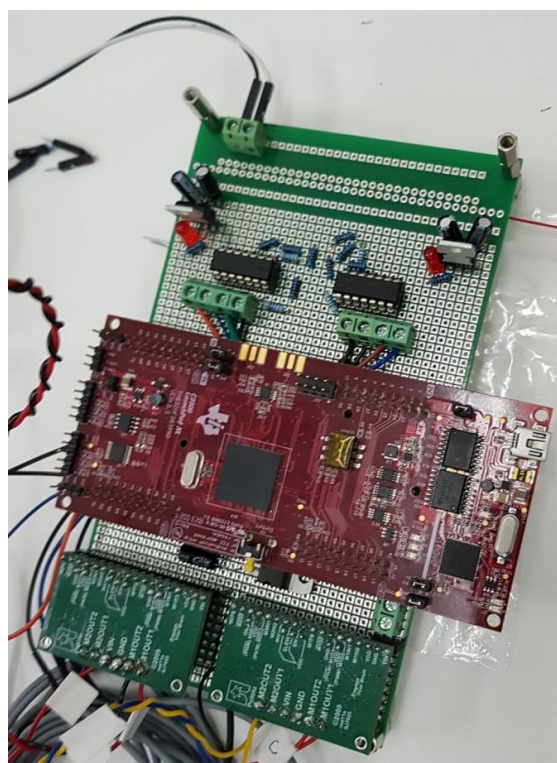


Figure 3.13. Control board of the test setup.

3.2. Test Setup

After testing with sub components of the system, the whole test system is constructed and assembled with the components described in the previous section. First, the magnetic bearing module is built as seen in *Figure 3.14*. This module has four electromagnets colored in orange and a ferrite permanent magnet colored in purple. The components are assembled to an acrylic part as a holder. It is chosen as Plexiglas not to interfere with magnetic field generated by the module.

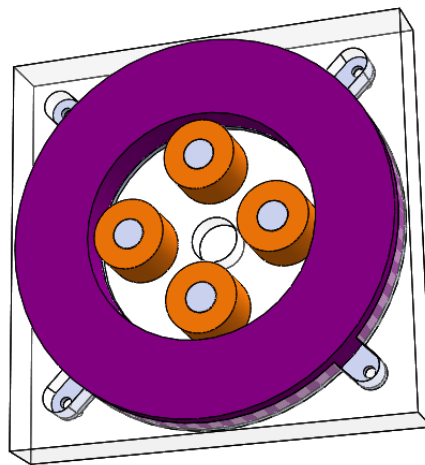


Figure 3.14. Magnetic bearing module of the test setup.

There are two magnetic bearing modules in the test setup to be able to levitate the rotor. The distance between permanent magnets in the modules is chosen to support the rotor in axial direction. The rotor construction is represented in *Figure 3.15*. It is placed in the center of the magnetic bearing modules.

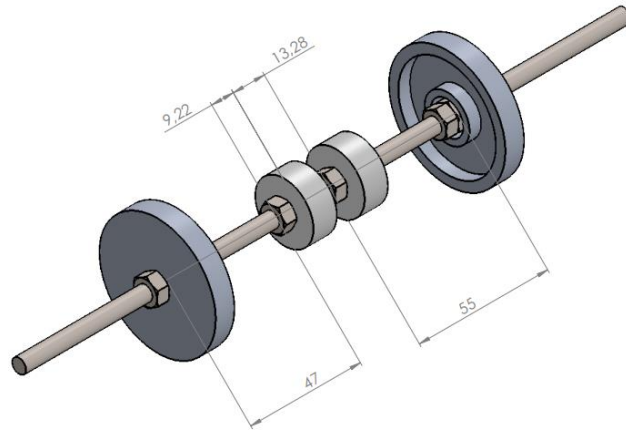


Figure 3.15. CAD model of the rotor and necessary dimensions.

The bottom ferrite magnet supports the whole weight of the rotor and counteracts against repulsive force of the upper ferrite ring magnet. In the axial direction with the help of both magnets and gravitational forces, a spring like preloading action is created on the rotor. In this setup, the rotor is axially symmetrical. However, in order for the bottom magnet to support the whole rotor weight, the bottom NdFeB magnet on the rotor is placed closer to ferrite magnet for higher force application. The asymmetrical dimensions can be seen in *Figure 3.15*. Moreover, the weight of the rotor and the inertia information about rotor assembly are taken from 3D CAD model.

Finally, the overall test setup 3D model is represented in *Figure 3.16* and the photo of the actual system is shown in *Figure 3.17*.

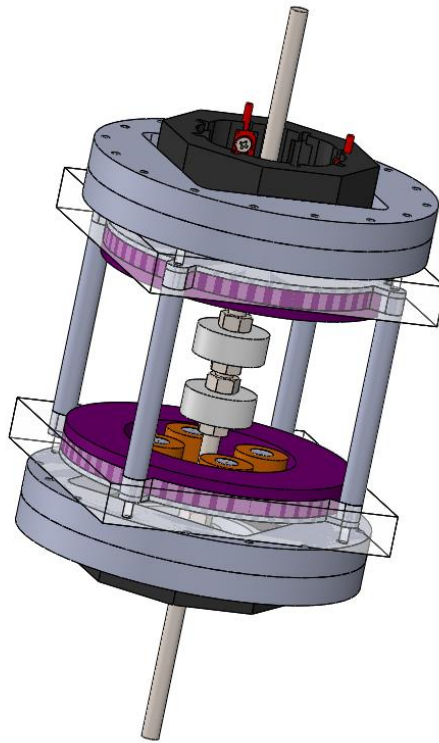


Figure 3.16. 3D CAD model of the test setup.

Unfortunately, there is no active element in the system so the damping of the rotor is very small in the axial direction. An additional damping mechanism or an active component (electromagnet) should be incorporated into design to improve damping in the axial direction.

In the radial direction, the position of the rotor is controlled by the active control action. The controller running at the TI F28379D processors applies PWM signals to the power amplifier so that the currents passing through the electromagnet coils can be controlled. There are four electromagnets on each side of the active magnetic bearings, as a result there are eight electromagnets in the test setup. On each magnetic bearing, the four electromagnets construct two orthogonal pole pairs and they can create radial forces on the NdFeB ring shaped rotor permanent magnets.

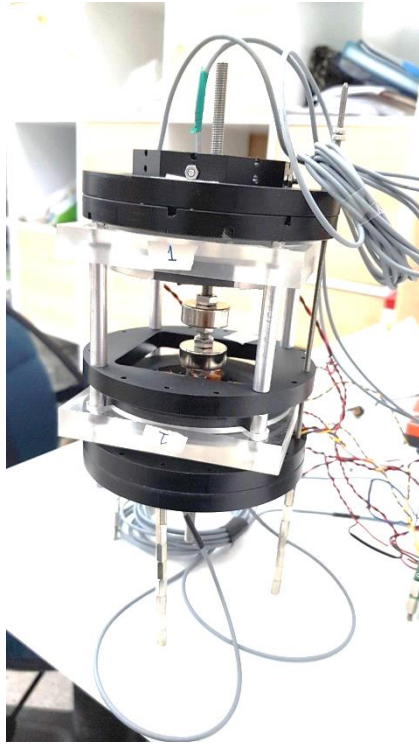


Figure 3.17. Photo of the actual test setup.

3.3. Mechanical Dynamics

In the test setup, as the rotor floats on active magnetic bearings, it is free to move in all six degrees of freedom. However, four active axes are considered as independent with each other, whereas the axial direction, which is the gravitational axis, is not taken into account because there is no active element or feedback element in that axis. In the vertical direction (axial), mainly the ferrite permanent magnets create a virtual stiffness to keep the rotor in position. Then, the controllable axes are radial directions at the top and at the bottom. Hence, the actuators are responsible for only the radial forces, which corresponds the radial displacements on the rotor permanent magnets. This active control action is creating the necessary restoring forces on the rotor in radial directions.

3.3.1. Equation of Motion

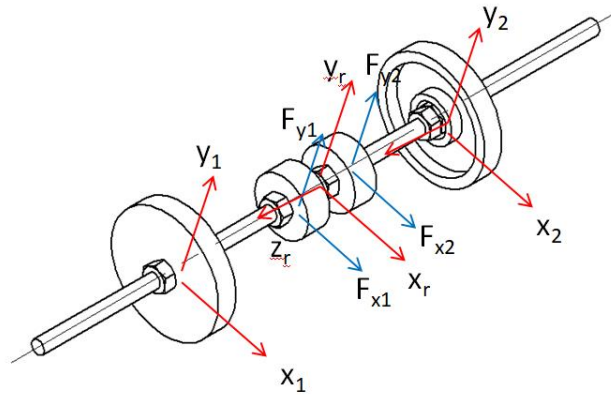
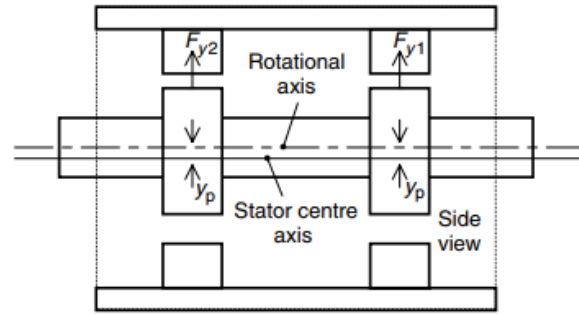


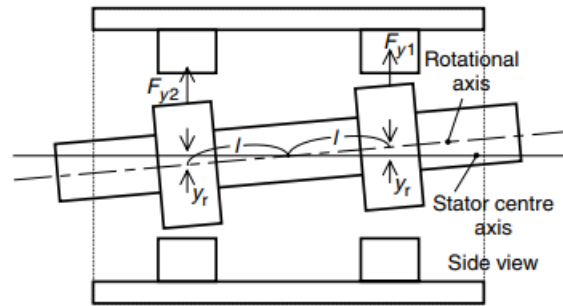
Figure 3.18. Forces and measurement axes on the rotor.

The forces acting on the rotor and sensor measurement locations are shown in *Figure 3.18*. The first radial bearing (numbered as 1) which is at the top generates radial forces F_{x1} and F_{y1} . The second one (numbered as 2) which is at the bottom generates radial forces F_{x2} and F_{y2} . However, the position measurements are taken in directions x_1 , x_2 , y_1 and y_2 . It should be noted that all of these axes are different from the axes x_r and y_r , which are the directions for center of mass of the rotor.

Chiba mentioned that the radial shaft movements can be expressed by translational and inclination movements as in *Figure 3.19*. It is considered as the axial axis of the rotor is moved in parallel to the stator's center axis in translational displacement. In the example figure, it is shown that both of the permanent magnets are moved by y_p . On the other hand, rotor shaft is rotated around the center of mass of the rotor and the displacement of the permanent magnets is y_r in *Figure 3.19* [15].



(a)



(b)

Figure 3.19. Active positioning (a) translational displacement; (b) inclination displacement.

Then, the radial movement is expressed by translational and inclination displacements as follows.

$$x_1 = x_p + x_r \quad (3.1)$$

$$y_1 = y_p + y_r \quad (3.2)$$

$$x_2 = x_p - x_r \quad (3.3)$$

$$y_2 = y_p - y_r \quad (3.4)$$

In the same way, the translational and inclination forces can be expressed in terms of radial forces of the magnetic bearings as follows.

$$F_{xp} = F_{x1} + F_{x2} \quad (3.5)$$

$$F_{yp} = F_{y1} + F_{y2} \quad (3.6)$$

$$F_{xr} = F_{x1} - F_{x2} \quad (3.7)$$

$$F_{yr} = F_{y1} - F_{y2} \quad (3.8)$$

The radial force is generated by both electromagnets. The dynamic motion equations for the translational movement should be taken into account with that. Hence,

$$\ddot{x}_p = \frac{F_{xp}}{m} + \frac{2k_x}{m} x_p \quad (3.9)$$

$$\ddot{y}_p = \frac{F_{yp}}{m} + \frac{2k_x}{m} y_p \quad (3.10)$$

For inclination movement, the dynamic equations are as follows [15].

$$\ddot{x}_r = -\frac{\omega_{rm} I_k}{I_i} \dot{y}_r + \frac{2k_x l_{rt}^2}{I_i} x_r + \frac{l_{rt}^2 F_{xr}}{I_i} \quad (3.11)$$

$$\ddot{y}_r = -\frac{\omega_{rm} I_k}{I_i} \dot{x}_r + \frac{2k_x l_{rt}^2}{I_i} y_r + \frac{l_{rt}^2 F_{yr}}{I_i} \quad (3.12)$$

Without gyroscopic effects, the above equations will be simpler because the rotor in the test setup is considered that it does not rotate. That means $\omega_{rm} = 0$

3.3.2. Magnetic Force Component Analysis

Through the dynamic motion equations, it should be noted that some of the parameters such as lengths, inertias and k_i , k_x magnetic constants of the systems. Lengths and inertia values can be detected easily with the 3D CAD model of the test setup. Moreover, magnetic analyses are performed by using finite element analysis methods in Ansys Maxwell environment.

First, some simplifications are made to reduce the calculation efforts in analysis. The only radial force contribution is from electromagnets on the permanent magnets in the rotor. Hence, one-axis force calculations are considered with two electromagnets and a NdFeB magnet. The air gap and the other specific dimensions are collected from 3D CAD model and suitable materials are selected. *Figure 3.20* shows the one axis actuation model with the direction of currents in electro magnets.

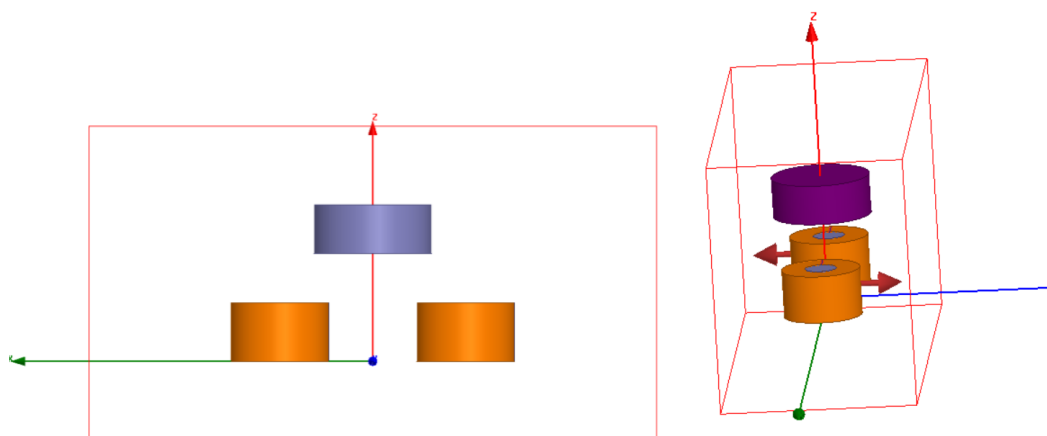


Figure 3.20. Modeling one axis actuation in finite element analysis method program Maxwell.

To be able to calculate the force current factor, the current values of the electromagnets are assigned as parametric and the analysis done in the range of 0.2 – 1.2 amperes by stepping 0.1 amperes. Corresponding force vs current graph is shown in *Figure 3.21*.

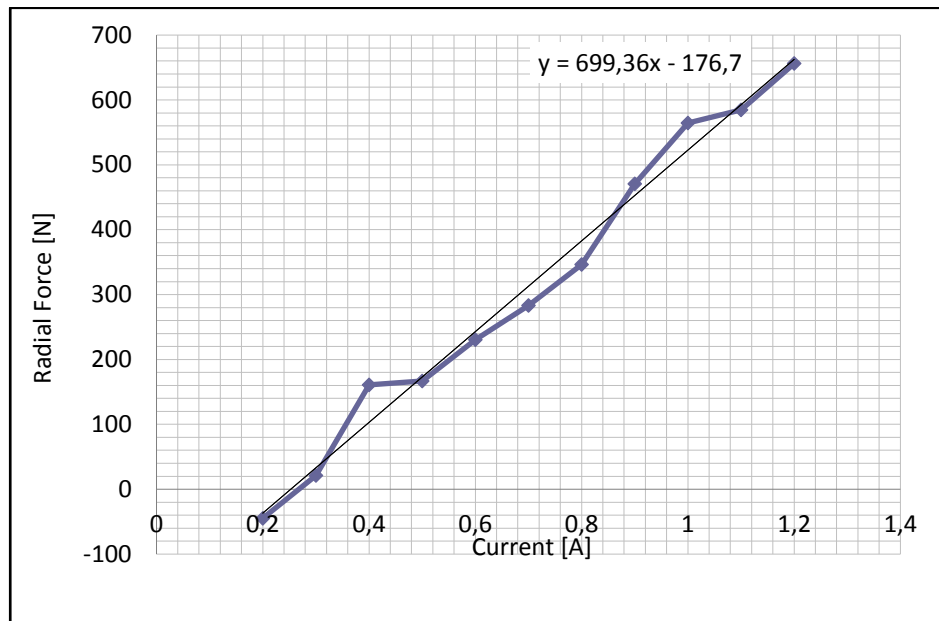


Figure 3.21. Graph of current vs radial force and linear equation.

Moreover, the force position factor, k_x , is also calculated in a similar way. The radial displacement is assigned in the range of 0.1 -0.5 mm by 0.05 stepping increment. The corresponding force vs displacement graph is shown in Figure 3.22

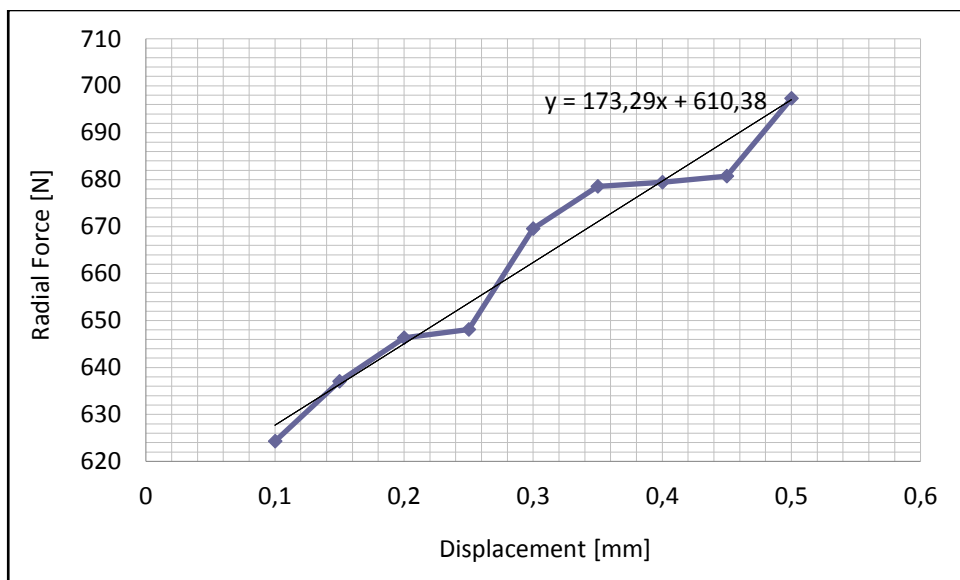


Figure 3.22. Graph of radial displacement vs radial force and linear equation.

It is known from Equation (2.24) that the corner frequency of the system is related with position factor and the mass of the rotor. Therefore, the corner frequency of the plant is calculated as follow.

$$\omega_c = \sqrt{\frac{k_x}{m}} = \sqrt{\frac{173.29}{0.181}} = 30.9 \frac{rad}{s} \quad (3.13)$$

Bode diagram of the plant is drawn in *Figure 3.23*. It can be seen in bode diagram that there is a decrease in the magnitude plot as 40dB/decade after 30.9 rad/s frequency value. It refers to second order term in the denominator of the transfer function.

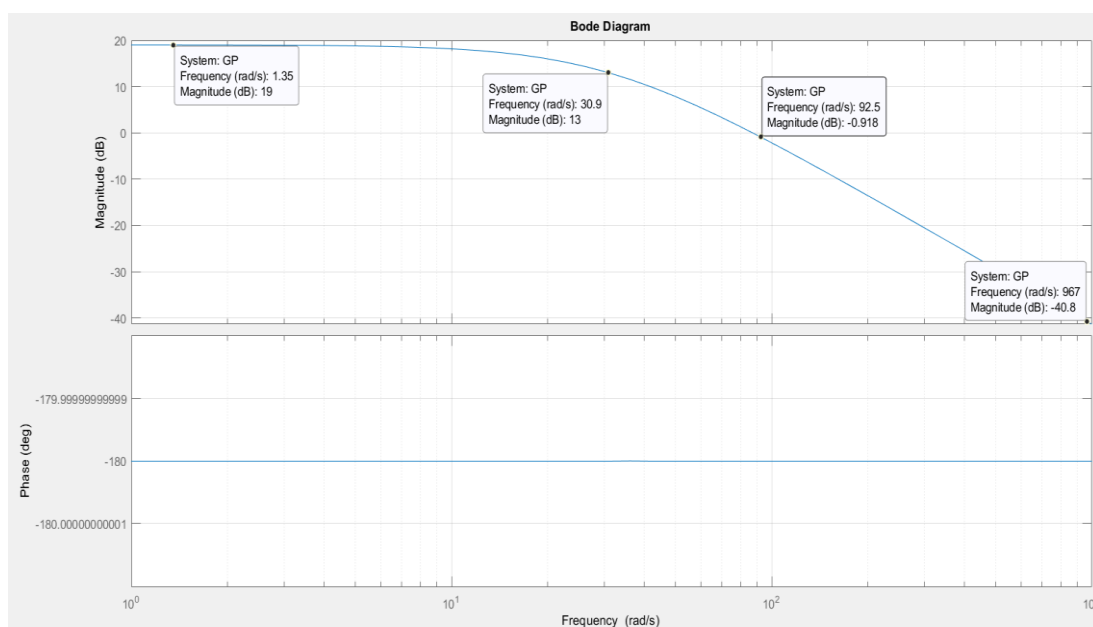


Figure 3.23. Bode diagram of the plant.

Bode diagram also shows the relation between current factor and position factor of the force. The magnitude can be calculated as follow.

$$M = 20 \log\left(\frac{k_i}{k_x}\right) = 19.05 \quad (3.14)$$

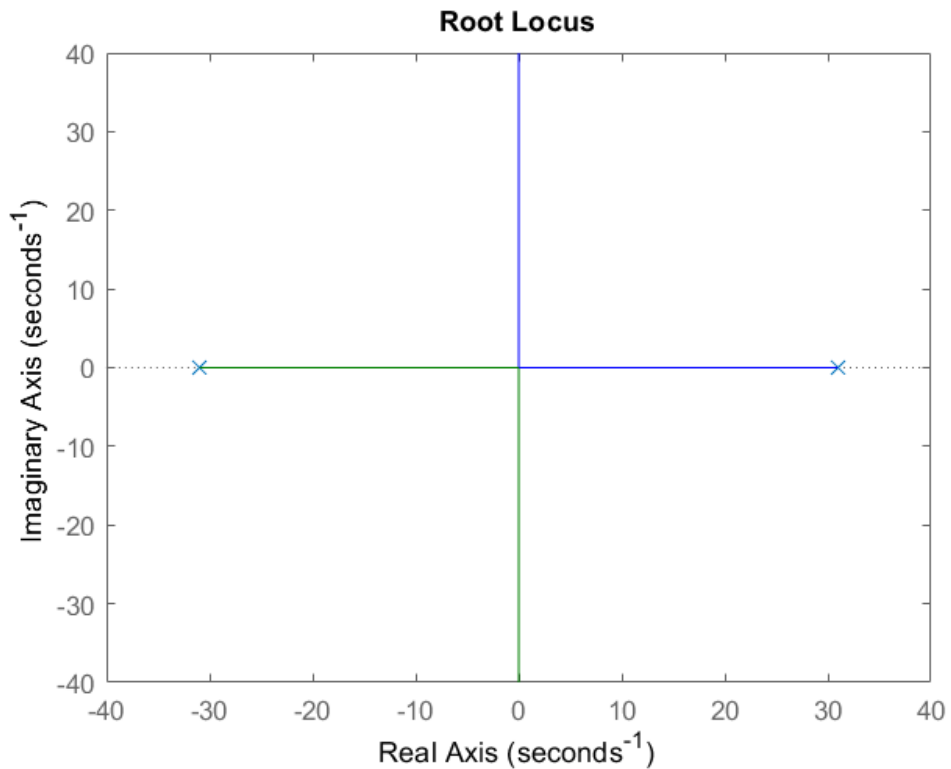


Figure 3.24. Root locus curve of the system.

Roots also can be seen in *Figure 3.24*. Root locus curve shows that the system is unstable with only a proportional gain because one of the pole is located on the left half plane. The roots are also calculated with corresponding Equation (2.24) in previous chapter. Even with the bigger proportional gain, the system can be named as marginally stable, which is practically unstable system.

Normally, the transfer function can be written as in the Equation (3.15) for a general second order system.

$$H = \frac{\omega_n^2}{s^2 + 2\zeta\omega_n s + \omega_n^2} \quad (3.15)$$

However, the transfer function for a magnetic bearing system is not have a damping coefficient due to nonexist damping term. Plant transfer function can be written again with the gathered constants as in the Equation (3.16).

In order to achieve the damping characteristic, controller is selected as in the Equation (3.17). With this controller, damping ratio is 0.71 and settling time is less than 0.1.

$$C = K_p + \frac{K_i}{s} + K_d s = \frac{0.05s^2 + 4s + 100}{s} \quad (3.17)$$

The step response of the open loop system with the controller and the bode plot is shown in the Figure 3.26. The comparison between the simulation results and experimental results will be discussed in chapter 4.

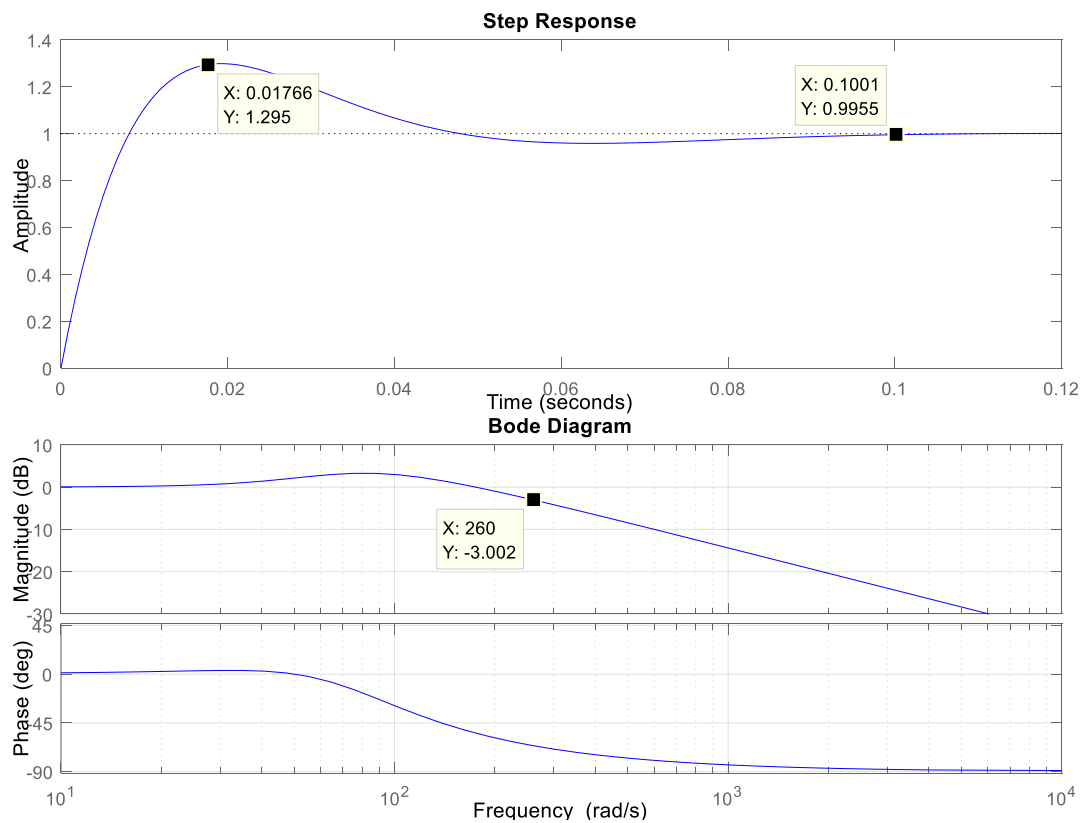


Figure 3.26. Step response and bode plot

From this design, it can be seen that the system bandwidth is 260 rad/sn which will be corrected with frequency tests in chapter 4.

3.4. Simulations

After finding the force factors in previous chapter, the translational portion of the displacement is modeled in the MATLAB Simulink environment. *Figure 3.27* shows the plant model of the system only for translational portion of the displacement. There are two actuators for one axis therefore the force factors are multiplied with two. There is also a disturbance force added in one of the radial directions of the system.

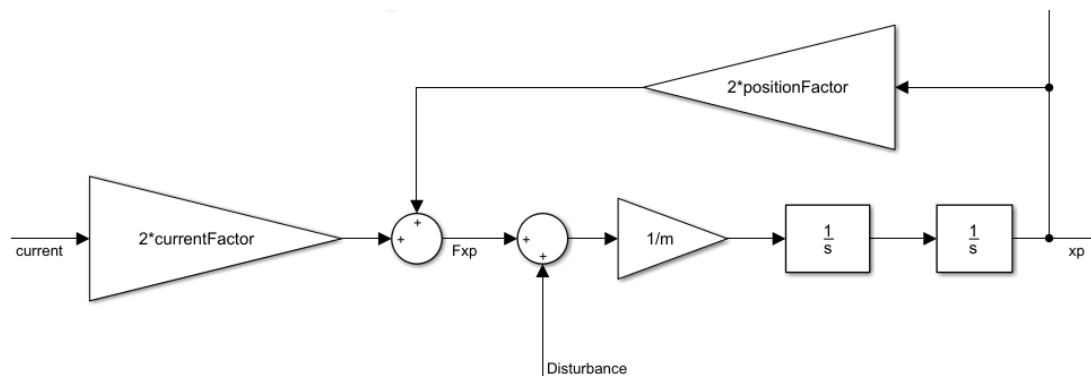


Figure 3.27. Plant model of the translational displacement component.

If a bias current or a disturbance is applied to the system then the position of the rotor is unstable as can be seen in *Figure 3.28*. The position output is increased dramatically, which means instability. Then, a controller should be added in simulations.

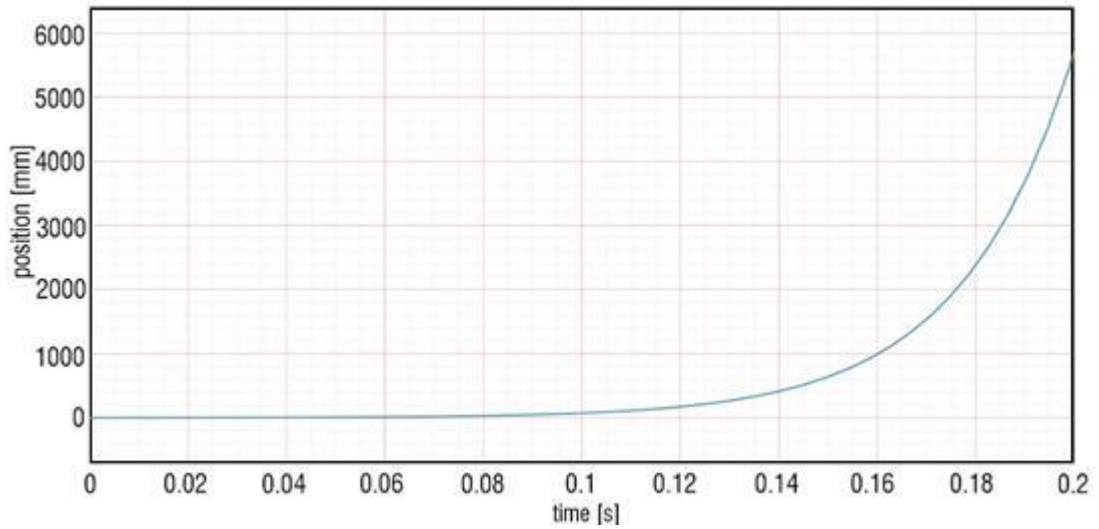


Figure 3.28. Position of the rotor under bias current.

The controller and the feedback are added to the simulations. The Simulink model of the overall feedback mechanism is shown *Figure 3.29*. In the test setup, controller in the DSP board manipulates the PWM signal of the amplifier of the motor driver. For this reason, the PWM to Voltage factor is added and a transfer function of the electromagnetic actuator is added in order to find out the current value in the electro magnets. The transfer function of the solenoids is taken as follow.

$$G_{solenoid} = \frac{1}{Ls + R} = \frac{1}{3.74 \times 10^{-3}s + 3.56} \quad (3.18)$$

The resistance and the inductance values are taken from *Figure 3.2*.

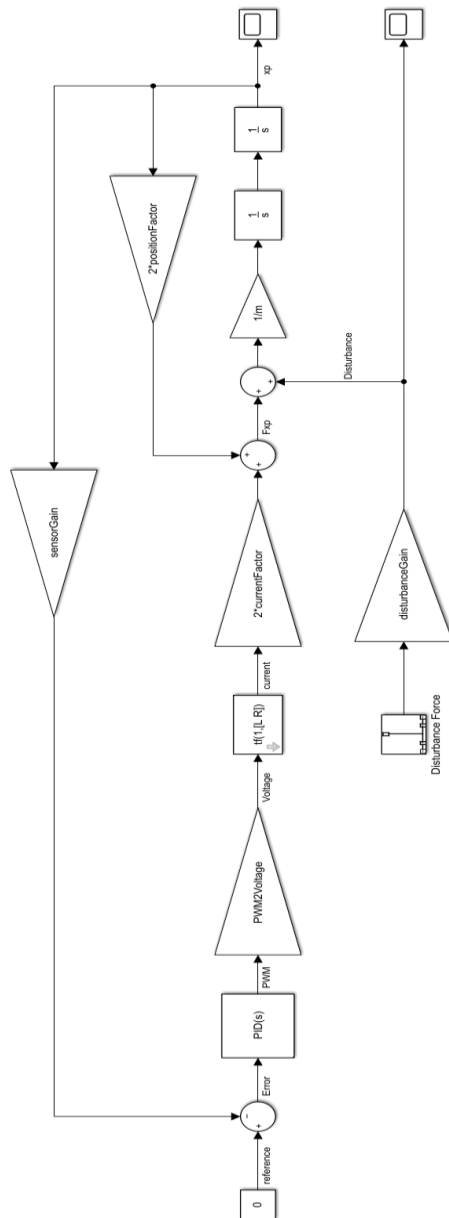


Figure 3.29. Overall system model in Simulink.

Moreover, the sensor gain is added. It is mentioned in previous section of the position sensor that the measurement range is 2mm corresponding to 13 volts. After the voltage division and ADC sampling of the processor board, a sensor gain is calculated in the tests and implemented into simulations.

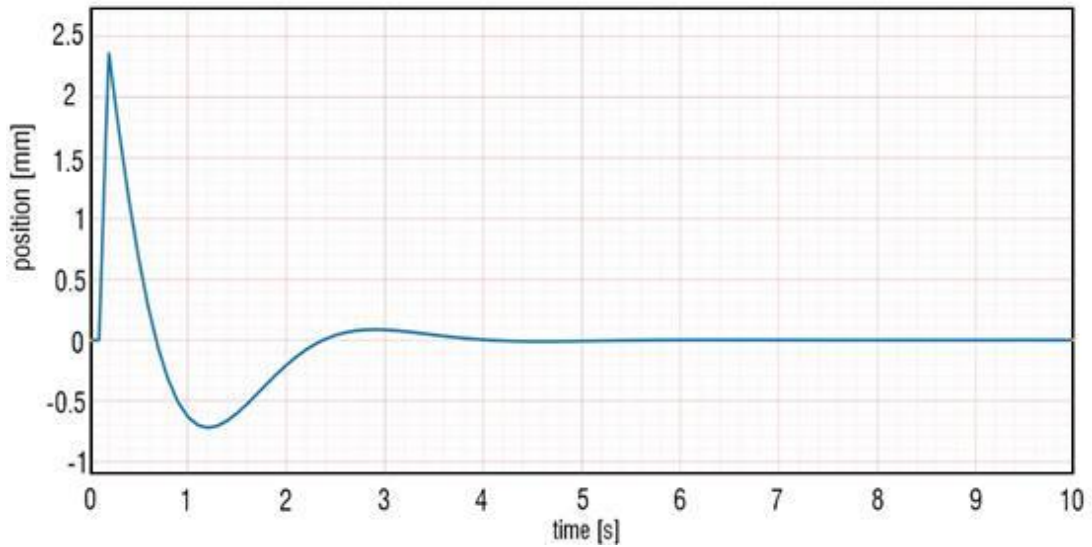


Figure 3.30. Simulation result of translational displacement.

One Newton disturbance force is applied after the controller and feedback are added to the system. The simulation result is shown in *Figure 3.30*. It can be said that the position of the rotor is stabilized with the added controller.

Rotational displacement portion can be included into the simulations after translational component is stabilized. By considering the asymmetry in the position of the center of mass along vertical axis, the rotational lengths of the top and bottom side of the rotor are taken into consideration. Moreover, the sensor readings are not from the directly the permanent magnets which is the axis of generated forces. Hence, the position measurement is also scaled to points where electromagnets apply forces. The lengths are shown in *Figure 3.15*. Corresponding Simulink model for both translational and rotational combination of displacement is shown in *Figure 3.31*.

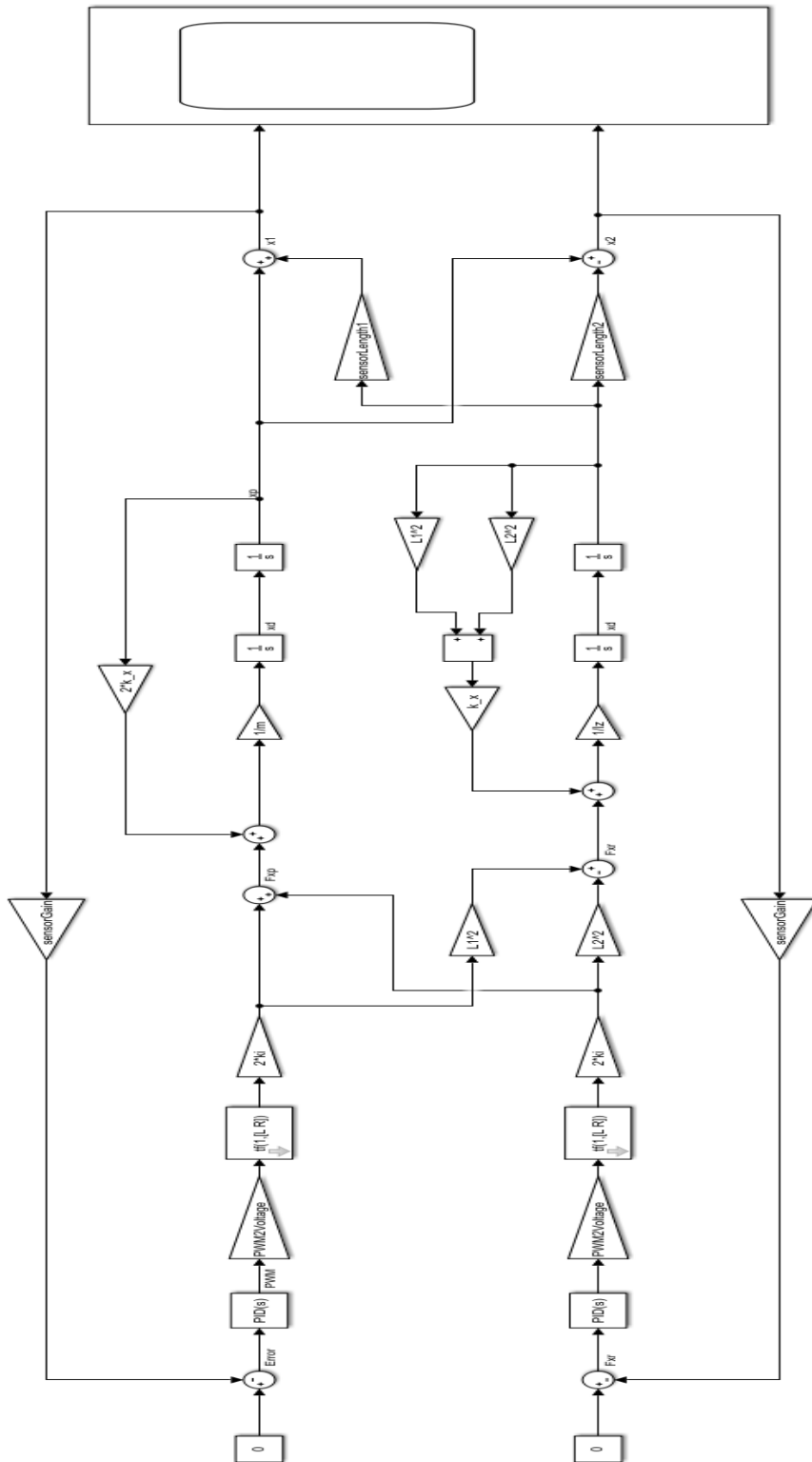


Figure 3.31. Simulink model of overall displacement model in one axis.

One newton disturbance force is applied in translational force part. The simulation result is shown in *Figure 3.32*.

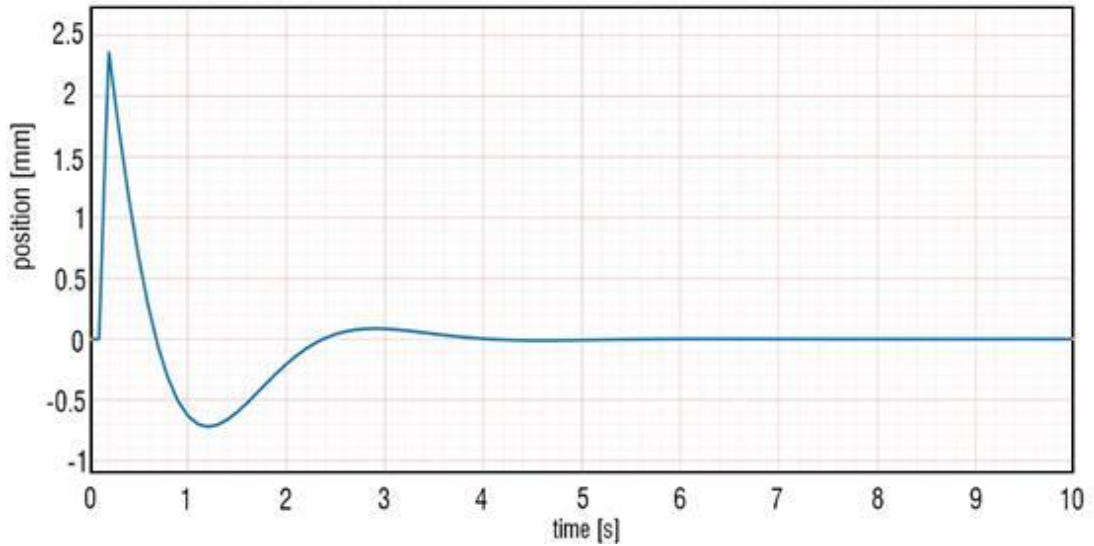


Figure 3.32. Simulation result of overall system, with translational disturbance.

The position measurements in upper and bottom side is the same as expected because only a translational disturbance is applied. After that, a rotational disturbance is applied and the result is shown in *Figure 3.33*.

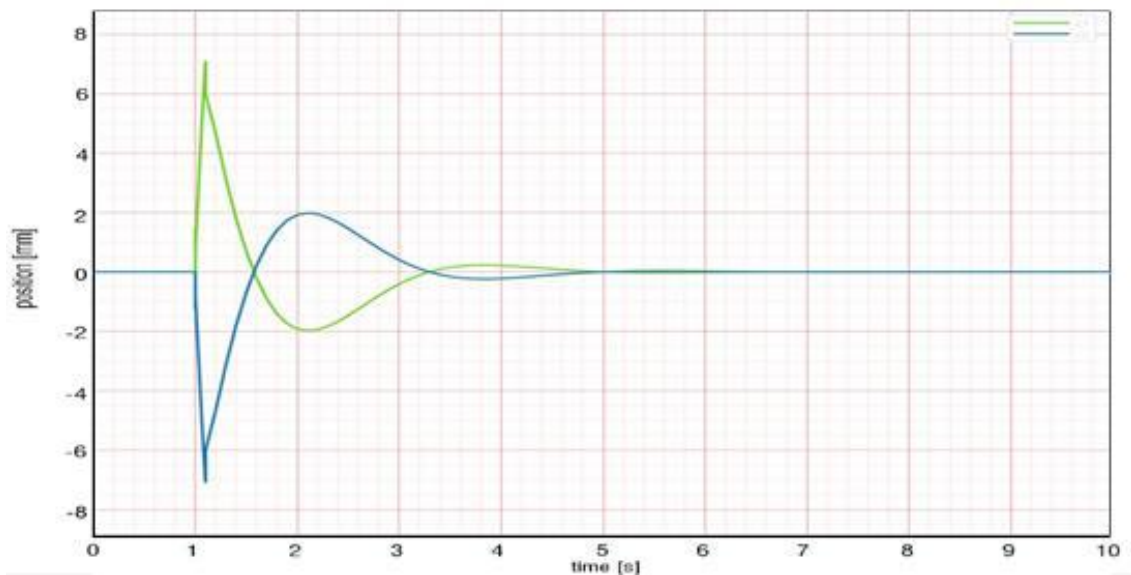


Figure 3.33. Simulation result of overall system, with rotational disturbance.

The measurements from the sensors have different signs as expected because of the rotational displacement. It is also seen that the effect of the rotational displacement is bigger than the translational displacement because the measurement points are far from the points that force applied.

The response time of the system is equal to each other when a translational or rotational disturbance applied. Settling time is five seconds for this system as seen in the result of simulations

Dynamic model in Simulink seem to be accurate and has a similar behavior with the real case as expected. Then, controller parameter should be investigated. *Figure 3.34* shows the output of the system with different proportional gains while other parameters are kept constant.

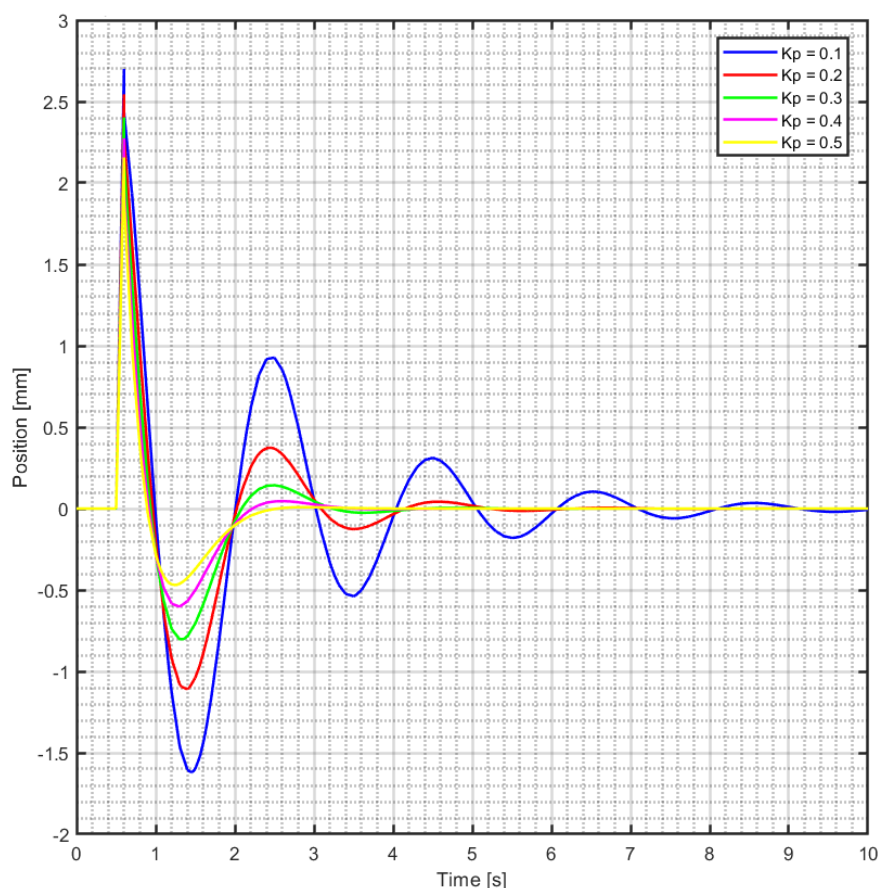


Figure 3.34. Simulation output with different proportional constants.

It can be seen in *Figure 3.34* that amplitude of the signal is decreased with increasing proportional gain constant. Moreover, settling time is also decreased with increasing gain.

Figure 3.35 shows the output of the system with increasing derivative controller gain while other variables are kept constant. It can be seen that the amplitude is decreased with increasing derivative gain constant too as in the proportional gain. However, settling time is increased with increasing derivative gain constant

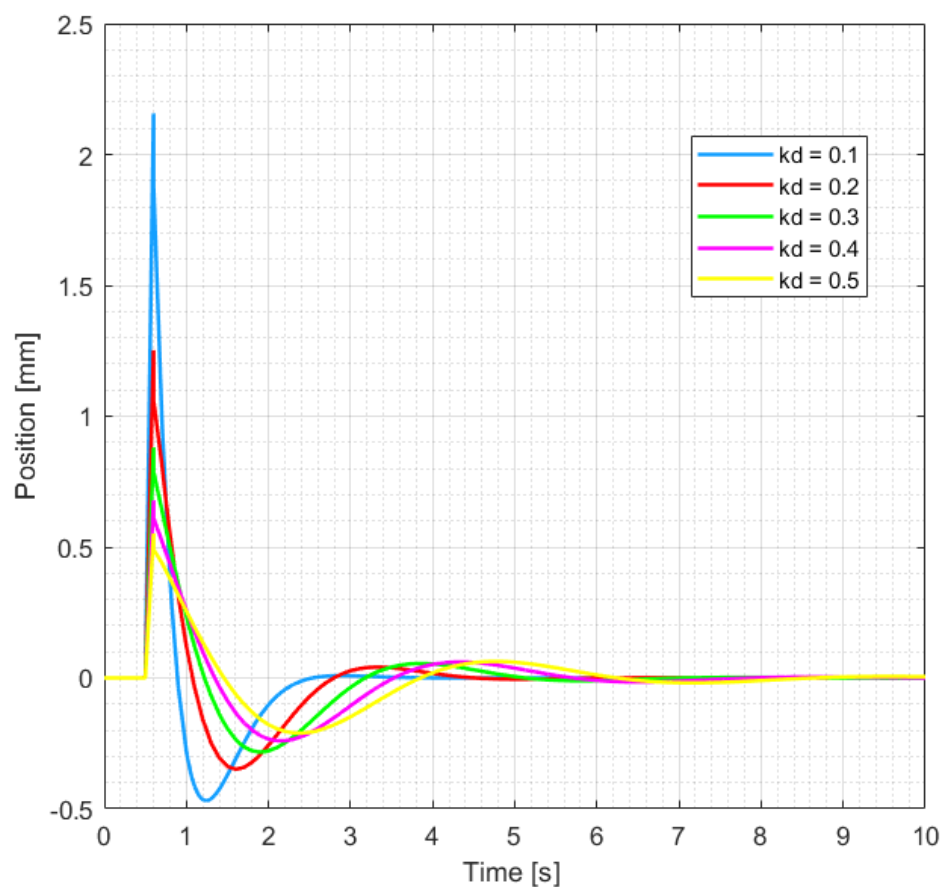


Figure 3.35. Simulation output with different derivative constants.

By looking at the simulation results, higher proportional and derivative gains are selected in order to be able to keep the rotor in its original position. Oscillations with high amplitudes are not preferred in the accelerometer design because the measurement range would be decreased by the overshoots in the system.

On the other hand, tuning such high gain values is rarely possible due to increased noise or amplifiers cannot stand the desired signal output even the processor demand. Therefore, fine-tuning should be necessary while experimenting with the test setup. The tests and final tuning results are given in the next chapter.

CHAPTER 4

PERFORMANCE EVALUATION

Some tests are conducted to gather information about the performance of the designed sensor. First, the PID controller and necessary blocks are included for such as saturation or integral windup in Simulink. Moreover, a helping software is designed in Simulink as a graphical user interface (GUI) to be able to tune the parameters easily and to collect the feedback signals.

Then, experiments are conducted to determine the performance of the sensor such as measurement limit or Allan Variance plot. Moreover, some comparisons are made with a commercial sensor, STIM300 inertial sensor, in order to evaluate the usability of the designed system.

4.1. Software Design for the Processor

4.1.1. Controller Implementation

The Eddy current sensors and current sensors feedbacks are collected via ADCs of the DSP board. Corresponding PWM outputs are selected to control motor driver. These implementations are easy with built-in blocks in Simulink as mentioned in previous chapter. An example of ADC sampling of the DSP board in Simulink is shown in Figure 4.1. Moreover, the PWM signal can be generated with ePWM block for C28 series DSP boards in Simulink. The corresponding ePWM block for one axis of the motor driver is shown in Figure 4.2.

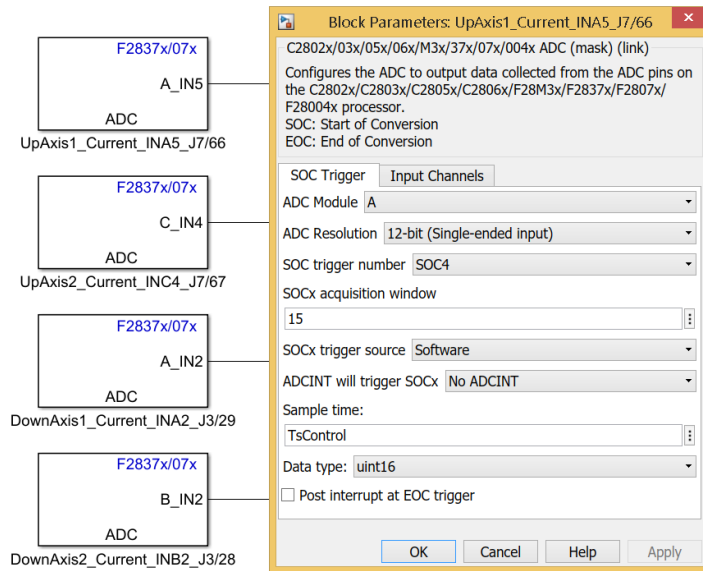


Figure 4.1. ADC sampling of c28 series DSP board for current feedback in Simulink.

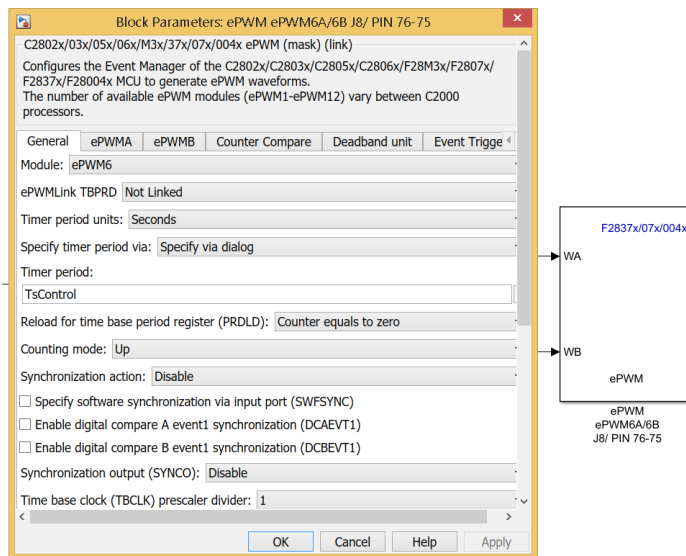
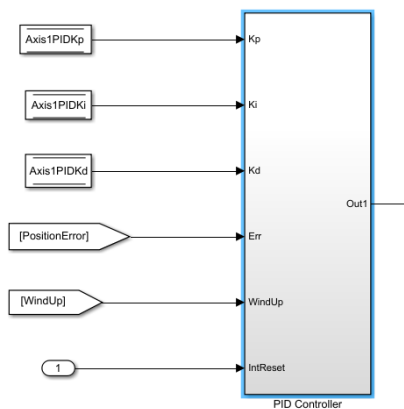


Figure 4.2. PWM signal generation in C28 series DSP board in Simulink.

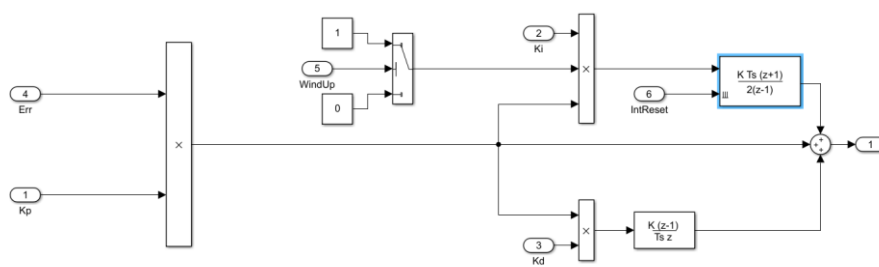
DSP board can be used with 100 kHz sampling frequency level. It is tested that 100 kHz sinus signal is generated by one of the DCA of the DSP board and read by one of the ADC of the DSP board again without any corruption in the signal. Moreover, it is also corrected via connecting an oscilloscope externally. However, Sampling

frequency of ADCs for feedback signals and signal generation for PWM outputs are selected to be 10 kHz because processor should also perform other task such as PID control and serial communication. A median filter also added to filter out the position sensor output. There is no need to add another filter to overcome the aliasing problem in discrete sampling because both high sampling rate (10 kHz) and median filtering are used to collect data from position sensors.

After feedback signal read out and PWM signal generation blocks included, a controller should be implemented into Simulink. Discrete integral and discrete derivative blocks are preferred rather than using built-in Simulink functions for PID controller. The designed controller with integral reset and integral windup can be seen in Figure 4.3.



(a)



(b)

Figure 4.3. Designed PID controller in Simulink.

A saturation block is included and a first order Butterworth filter is implemented to the output of the controller in order to carry smooth and more accurate signals to the PWM blocks.

Integral wind up is activated when the corresponding controller output is saturated and integral reset is activated when a parameter of the one of the controller is changed.

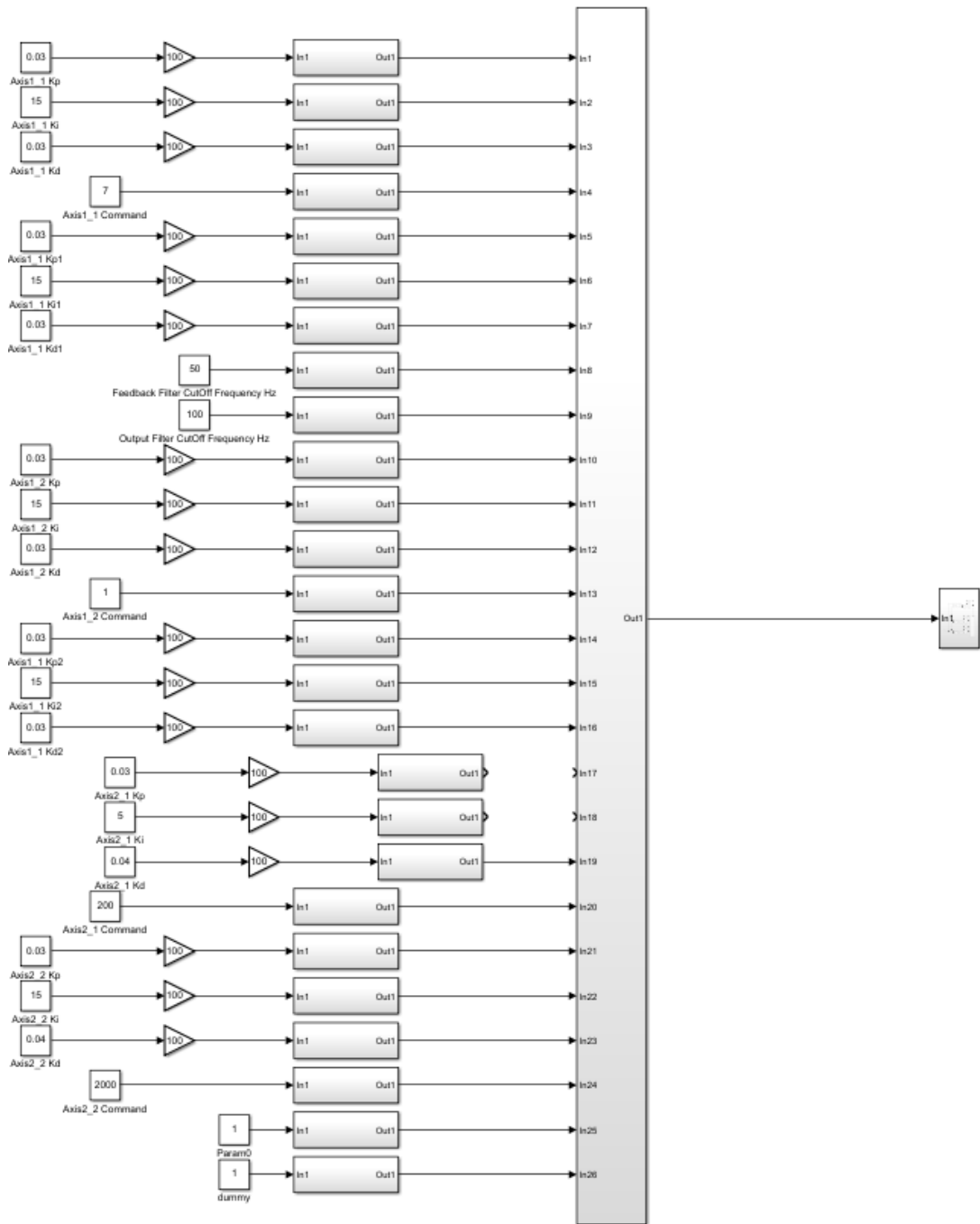
4.1.2. Communication with DSP Board

User can easily communicate with DP board via serial communication. This serial communication is transferred to the board with USB thanks to the included FTDI chip in the board. This also brings the isolation of DSP chip from the computer.

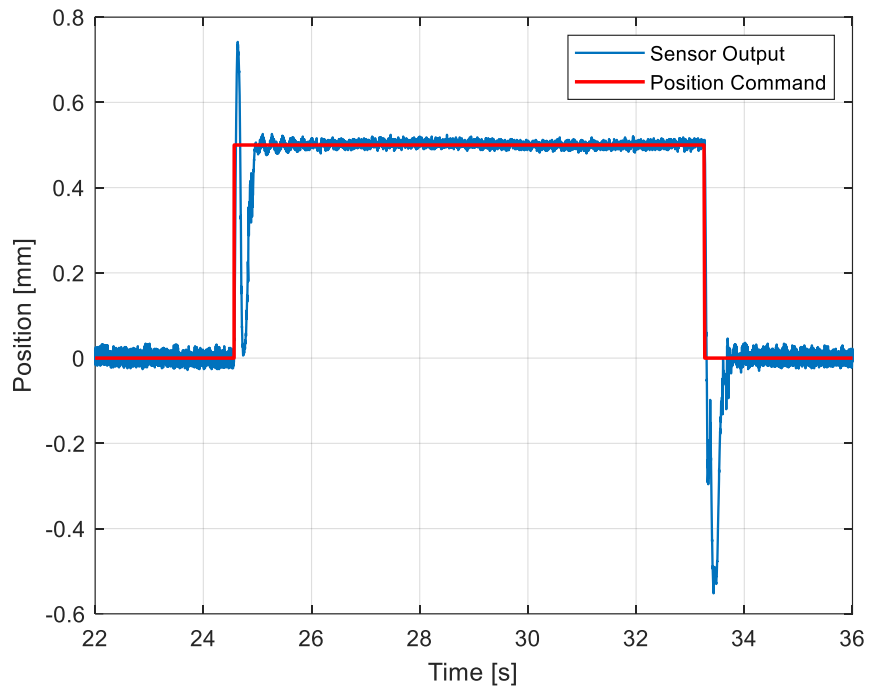
A serial communication protocol is implemented with two bytes header and one-byte counter in the beginning and one-byte checksum at the end. There are four signals in between these bytes. Signals are converted two uint16 data types. The number of the signals can be increased but then the serial communication speed should be decreased from 1 kHz.

On the other hand, another receiver software should be designed to collect this serial communication packages from DSP board and control whether the signal is valid or not. Then signals should be parsed and multiplied with a scale factor to get a meaningful output.

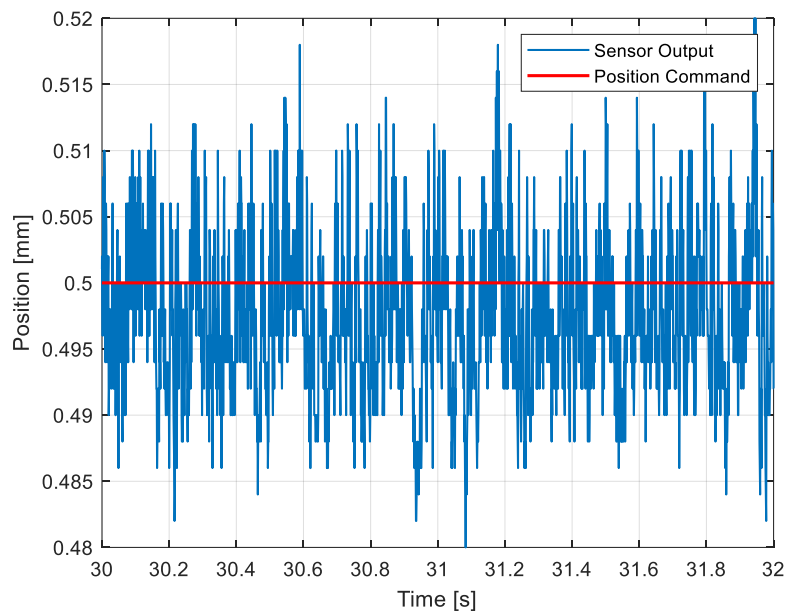
A transmitter is added to communication software to change the controller parameters and cut off frequency values of filters while tuning. The signals are ordered and packaged into DSP. User can also change the output signals of the DSP board by sending a package number to the DSP board. In order to send the necessary parameters to the DSP board and collect the feedback signals from the DSP board a GUI is designed as seen in Figure 4.4.



(a)



(a)

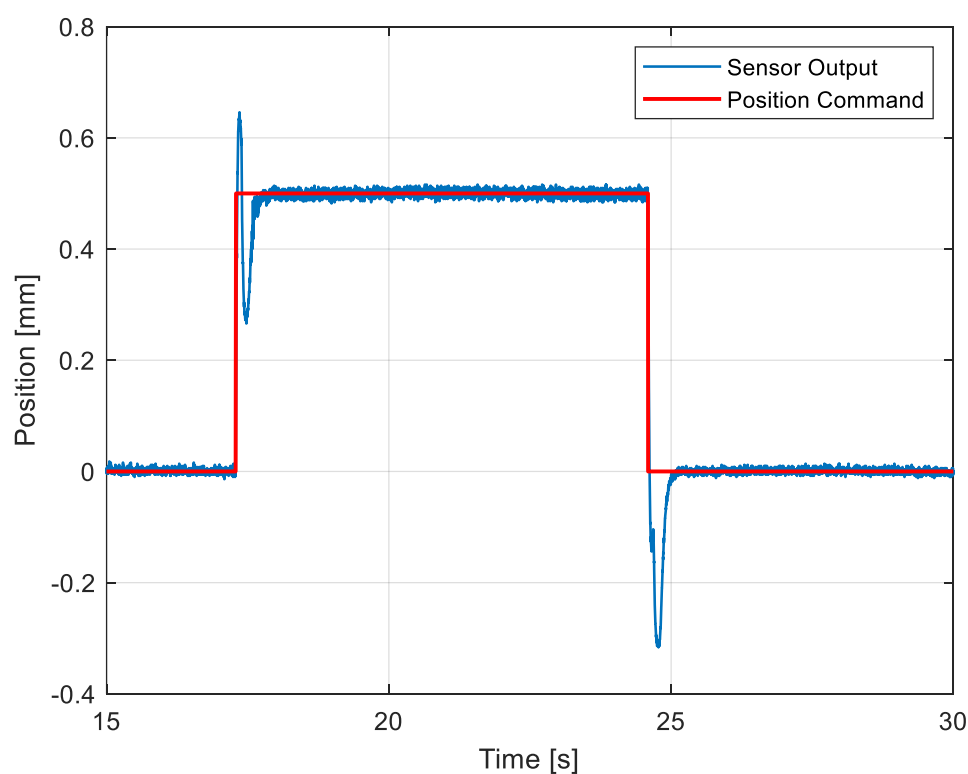


(b)

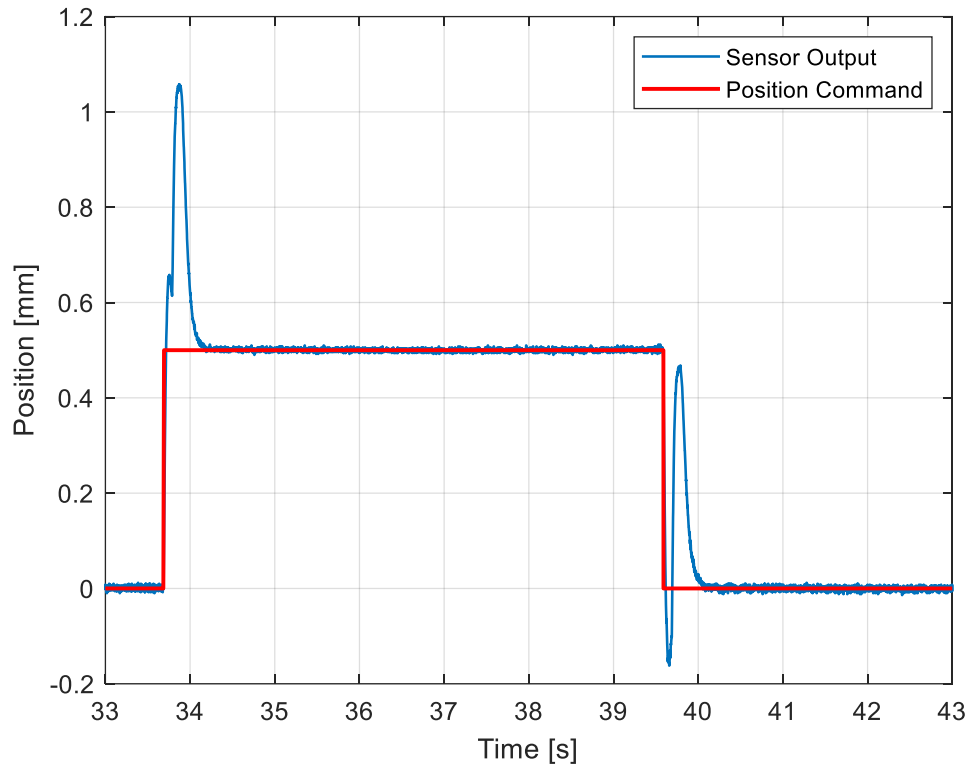
Figure 4.5. (a) Step response of the system; (b) noise due to Eddy current sensor.

By examining the step response of the system, parameters are iterated for optimal values. Figure 4.5 shows the system response with a step position command. Amplitude of the command is 0.5 mm, which is the half of the range of the system because rotor can move in radial axis in 1 mm only. There is an overshoot due to integral term however, it is essential to decrease rise time.

All actuators and all axes are assumed to have same behavior however; it is not the same in practice. There are many differences in the dynamics of the axes. For example, air gap is not exactly the same in all axes or position of the actuators may be eccentric due to machining of the holder etc. Because of these types of uncertainties, behavior of the radial axes in horizontal plane is not the same. This difference can be seen by comparing the graphs in Figure 4.6



(a)



(b)

Figure 4.6. (a) Step response of the X-axis; (b) Step response of the Y-Axis.

By looking the behavior of all axes, a common parameter set is selected for all PID controllers. However, it can be concluded from the step responses of axes that the bottom side has a better performance. Hence, higher controller parameter values can be selected for the axes in bottom side. It can be explained that the air gap in between the electromagnets and neodymium magnets is smaller than upper side. Therefore, the force capability of bottom actuators is higher than upper ones.

4.3. Comparison with a Commercial Sensor

4.3.1. STIM300 Acceleration Sensor

STIM300 is a MEMS based and tactical grade IMU from SENSOROR. This sensor is widely used for one of the firm in defense industry in Turkey. Therefore, it is selected to compare with the designed magnetically levitated accelerometer. The accelerometer and inclinometer specification of the IMU is taken by datasheet[26] as in Table 4.1 and the axis definition of the IMU is shown in Figure 4.7.

Table 4.1. Parameters of STIM300 IMU [26].

	Value	Unit
ACCELEROMETER		
Input Range	± 10	g
Resolution	1.9	μg
Bias instability	0.05	mg
Velocity random walk	0.07	m/s/ $\sqrt{\text{h}}$
Bias error over temperature gradients	± 2	mg rms
Scale factor accuracy	± 300	ppm
INCLINOMETER		
Input Range	± 1.7	g
Resolution	0.2	μg
Scale factor accuracy	± 500	ppm

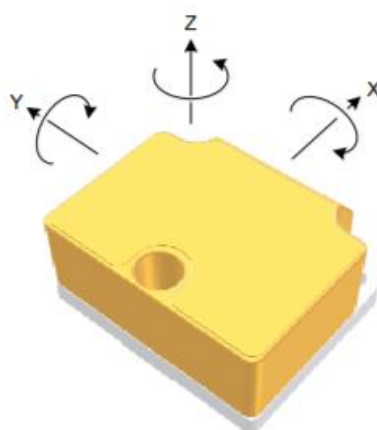


Figure 4.7. Axis definition of STIM300 IMU.

4.3.2. Tests with STIM300 and Designed Accelerometer

Figure 4.8 and Figure 4.9 show the comparison of the designed sensor with a commercial sensor, STIM300. The collected test data from the test data is filtered and scaled by looking the commercial sensor output. It can be seen in the test result that designed sensor measurements follows very close to the measurement of the STIM300 sensor under high frequency disturbances. The disturbance period is seen as 0.15 seconds in Figure 4.8.

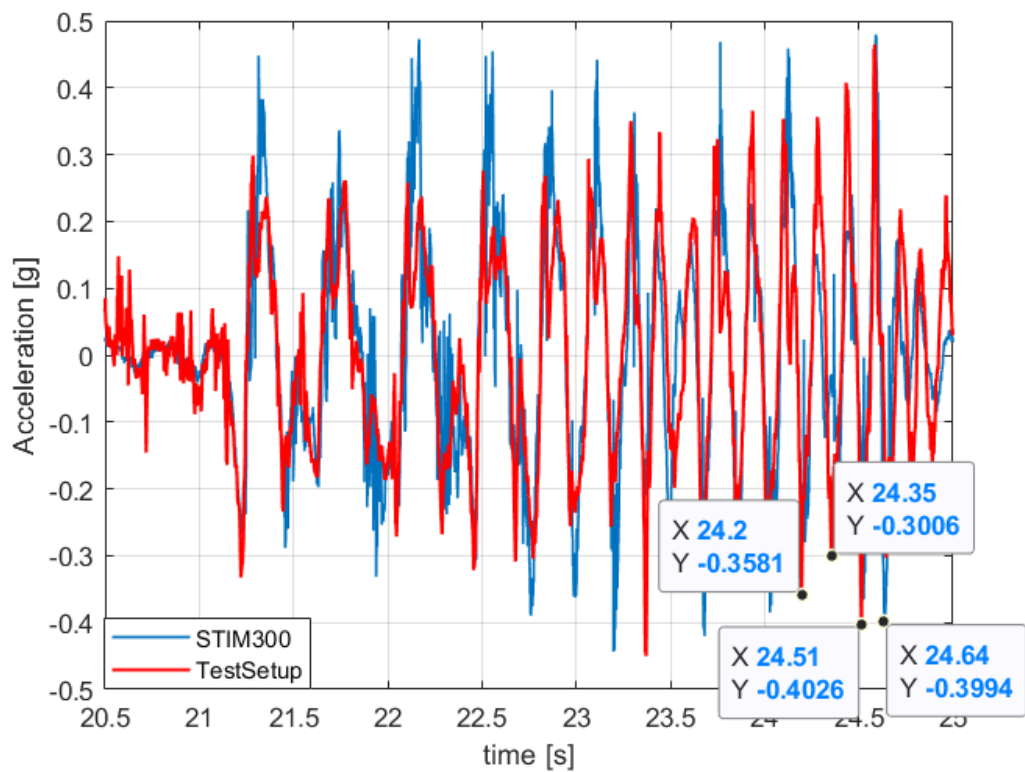


Figure 4.8. Comparison with commercial sensor in x-axis.

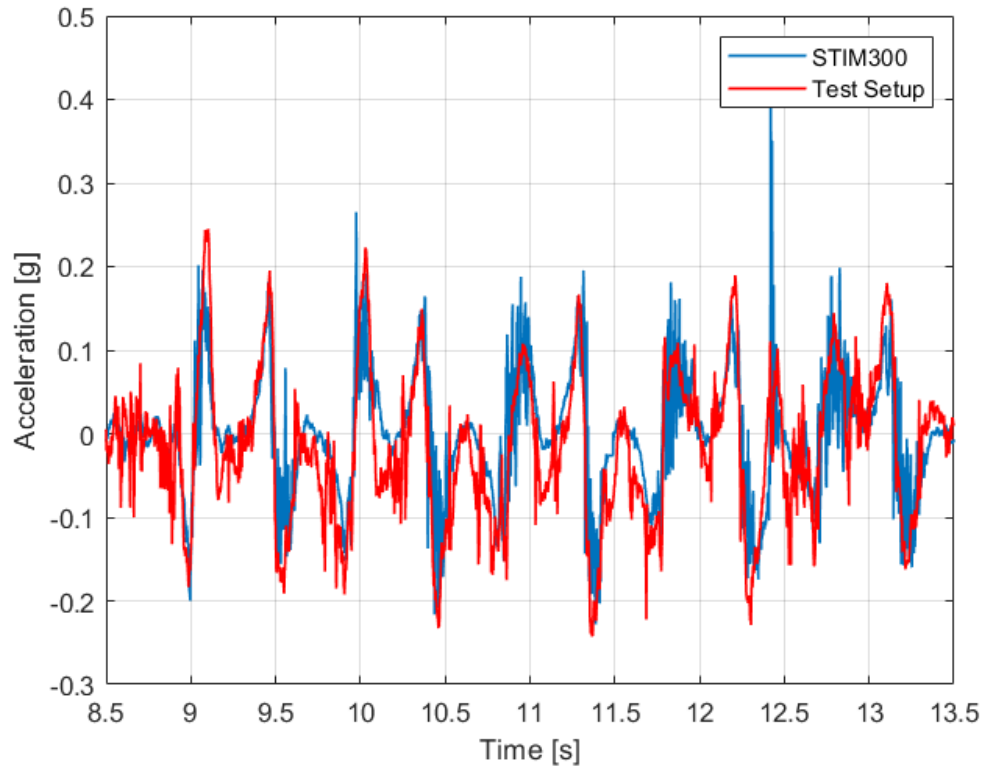


Figure 4.9. Comparison with commercial sensor in y-axis.

4.4. Measurement Limit

The test setup is rotated to be able to determine the measurement limit of the designed sensor. Figure 4.10 shows the result of this experiment. After 0.6 g values, sensor cannot achieve an accurate measurement. However, until the 0.6 g level the measurement is consisted with commercial sensor. Therefore, it can be said that the maximum acceleration value, which the designed sensor can measure, is 0.6 g.

Figure 4.11 shows also that test setup can measure more than 0.6 g acceleration values. Moreover, STIM300 sensor has a high frequency and low amplitude noise in high acceleration values however; test setup has a low frequency but high amplitude noise in low acceleration values.

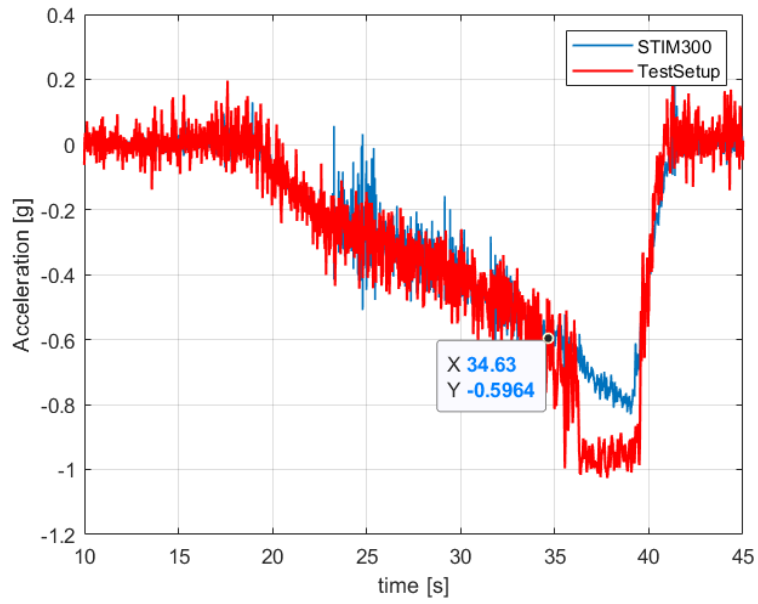


Figure 4.10. Rotation test.

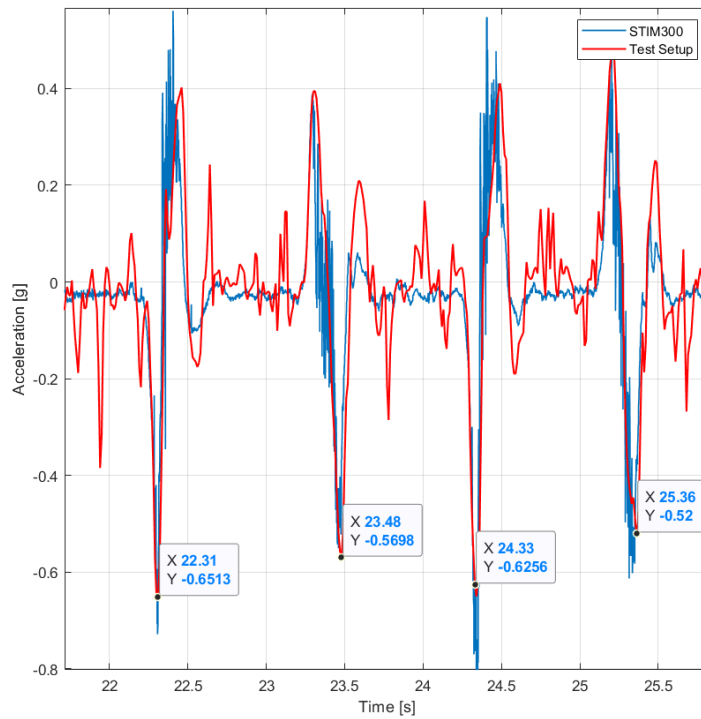


Figure 4.11. Comparison with commercial sensor, maximum value.

4.5. Allan Variance of the Test Setup

Allan variance is a common method used to identify noise level in inertial sensors such as accelerometers or gyroscopes. There are various noise types. The Allan Variance plot is generally used to determine the bias instability and random walk (white noise) of a sensor [27]. For example, STIM300 has a bias instability as 0.05 mg and velocity random walk as 0.07 m/s/ \sqrt{h} .

The acceleration data is collected in five minutes without applying any disturbance on the system. The Allan Variance is plot by the help of MATLAB script shared in Appendix. Corresponding graph is shown in Figure 4.12.

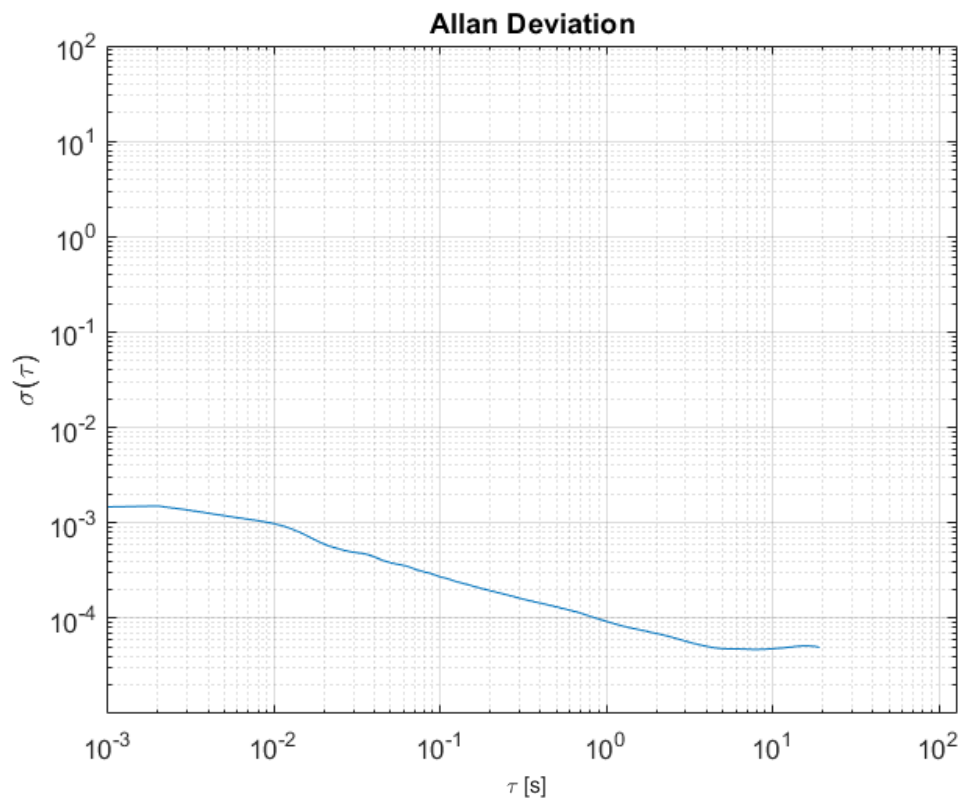


Figure 4.12. Allan Variance plot of STIM300.

By looking of the Allan Variance, one can determine the bias instability and random walk. A line with a 0.5 slope for random walk and a line with a 0 slope is added to the graph. The points where the corresponding values are gathered is marked in Figure 4.13.

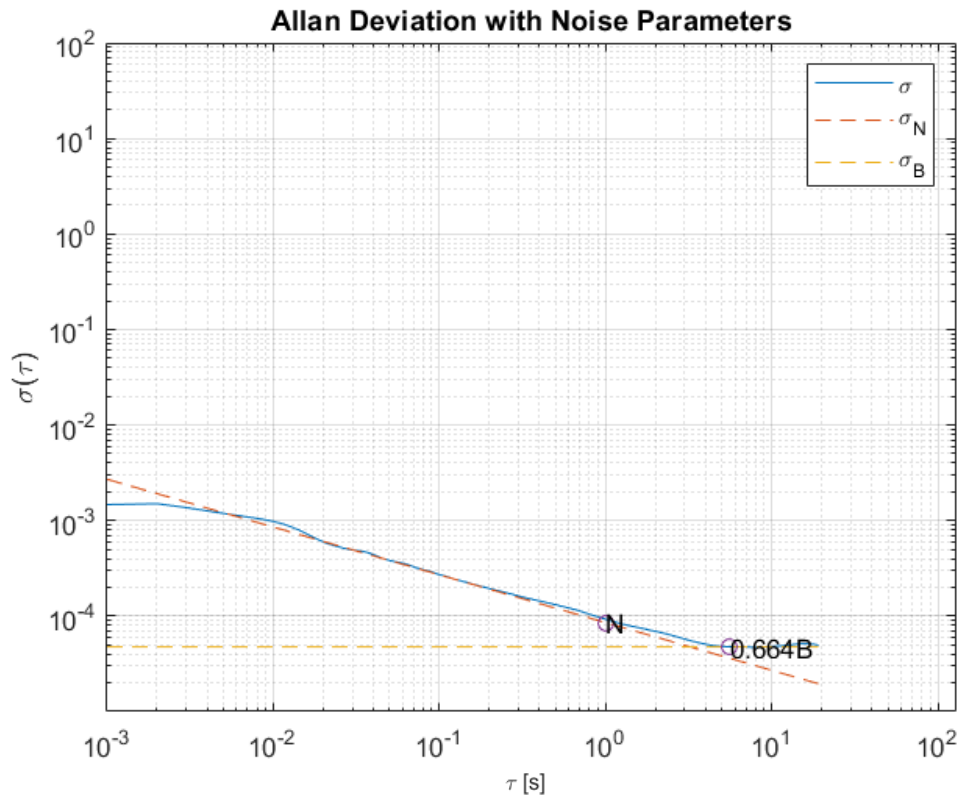


Figure 4.13. Random walk and Bias instability of STIM300.

Calculated value for random walk of STIM300 is 0.0498 m/s/ \sqrt{h} and for bias instability is 0.0072 mg from the collected data in five minutes. These values are very close to the given values in the datasheet of STIM300.

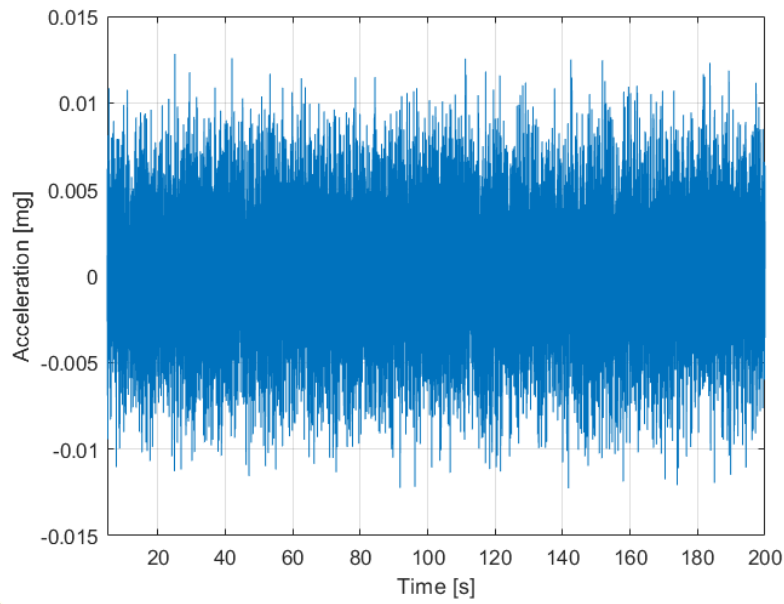


Figure 4.14. Collected data from designed accelerometer for Allan variance calculation.

Test is repeated to get the Allan Variance plot of the designed accelerometer. Data is collected from test setup in five minutes without applying any disturbance. Collected acceleration information from designed sensor is shown in Figure 4.14. Same script is used to draw Allan Variance plot. The resulted graph can be seen in Figure 4.15 and lines for random walk and bias instability are shown in Figure 4.16.

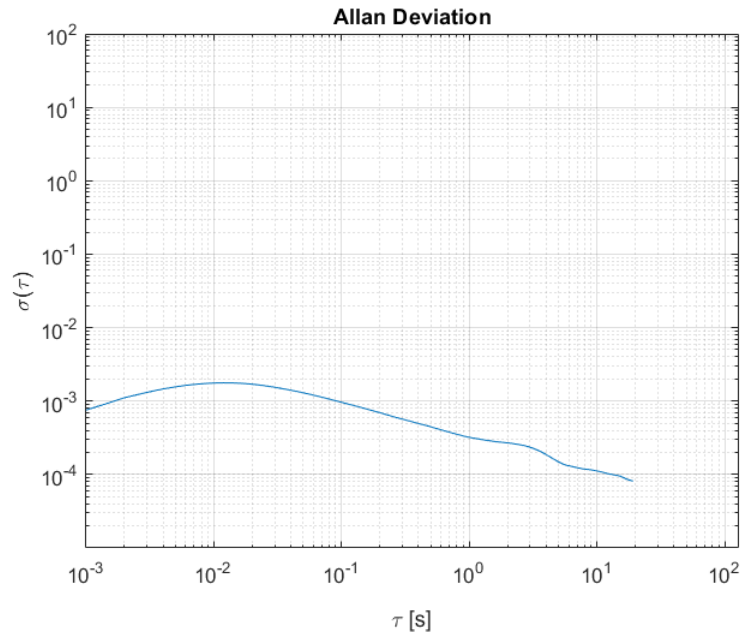


Figure 4.15. Allan Variance plot of designed accelerometer.

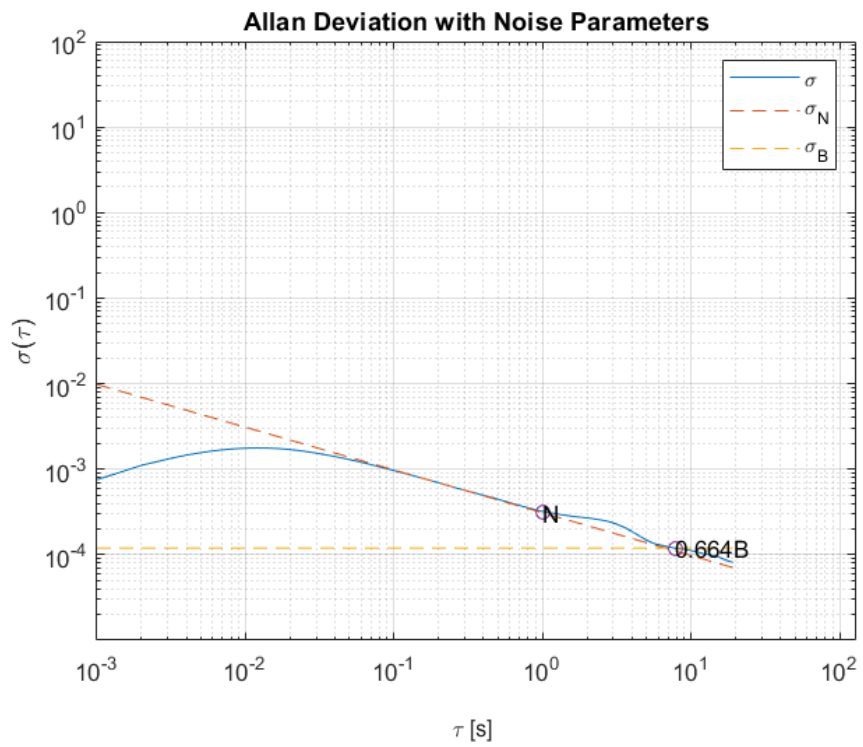
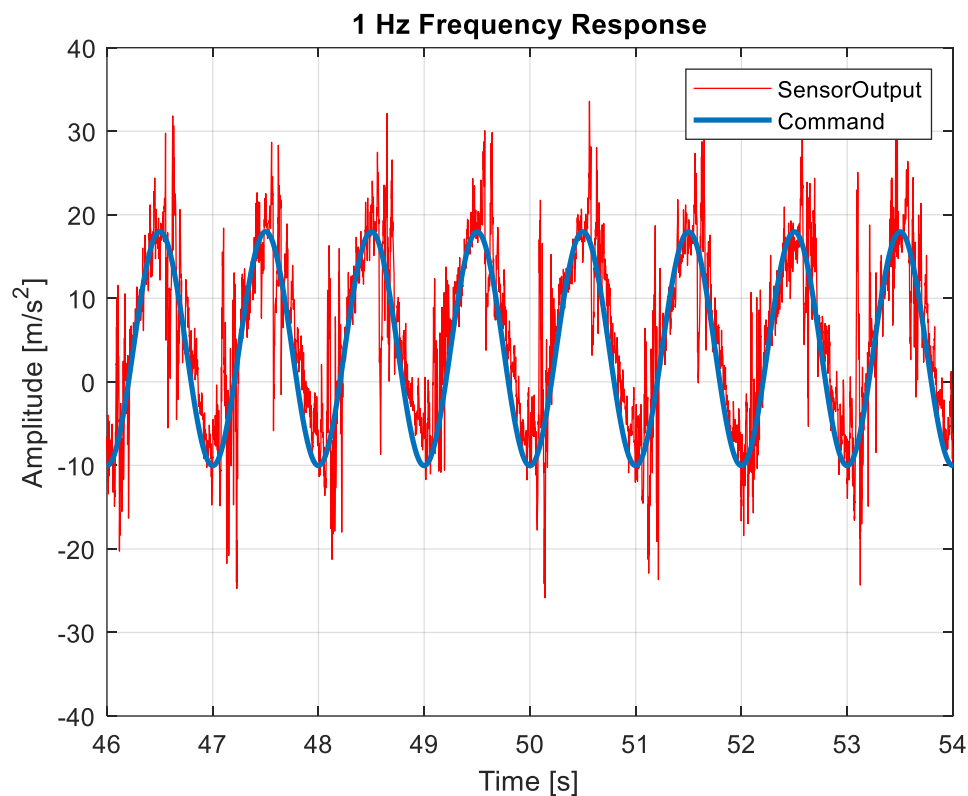


Figure 4.16. Random walk and Bias instability of designed accelerometer.

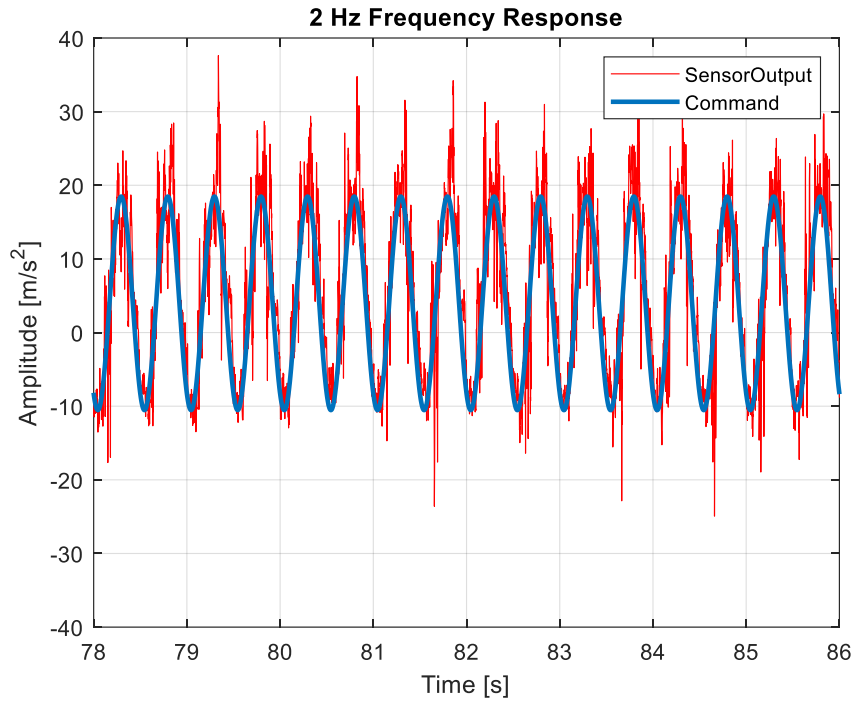
Calculated value for random walk of the designed accelerometer is $0.182 \text{ m/s}/\sqrt{\text{h}}$. Calculated value for bias instability is 0.174 mg . These values are a bit higher than STIM300 because of the high noise contribution from position sensor in the test setup. By improving the position feedback sensor, these values can be better.

4.6. Frequency Test

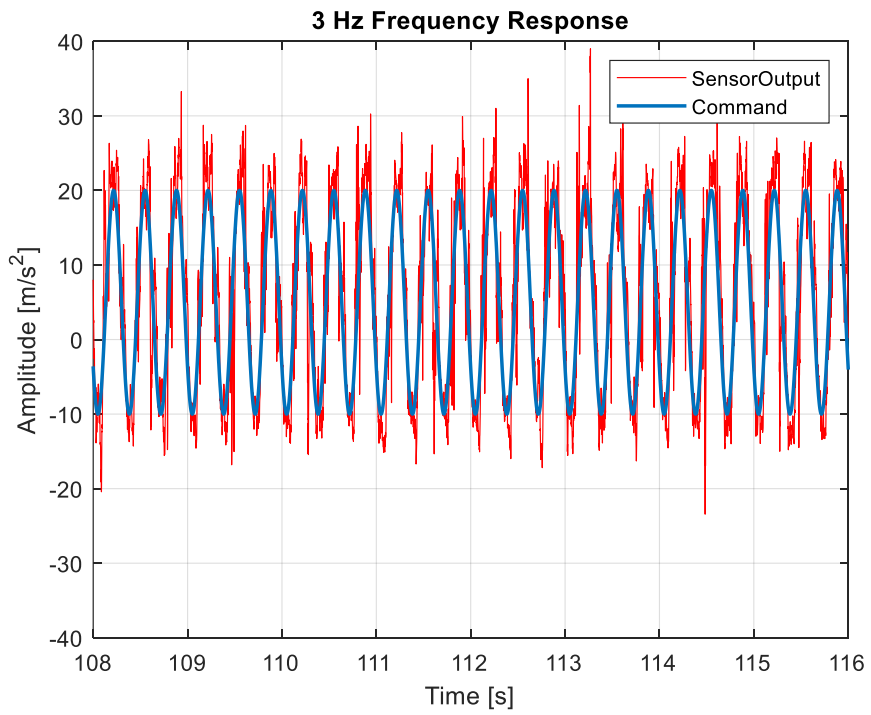
The test setup is mounted onto a six DOF Stewart Platform to actuate the system with different frequency values. The platform is actuated with sinusoidal commands between 0.25 to 10 Hz. Only 1 to 5 Hz frequency response plots are shown in Figure 4.17 overall result will be shown in bode plot in Figure 4.18.



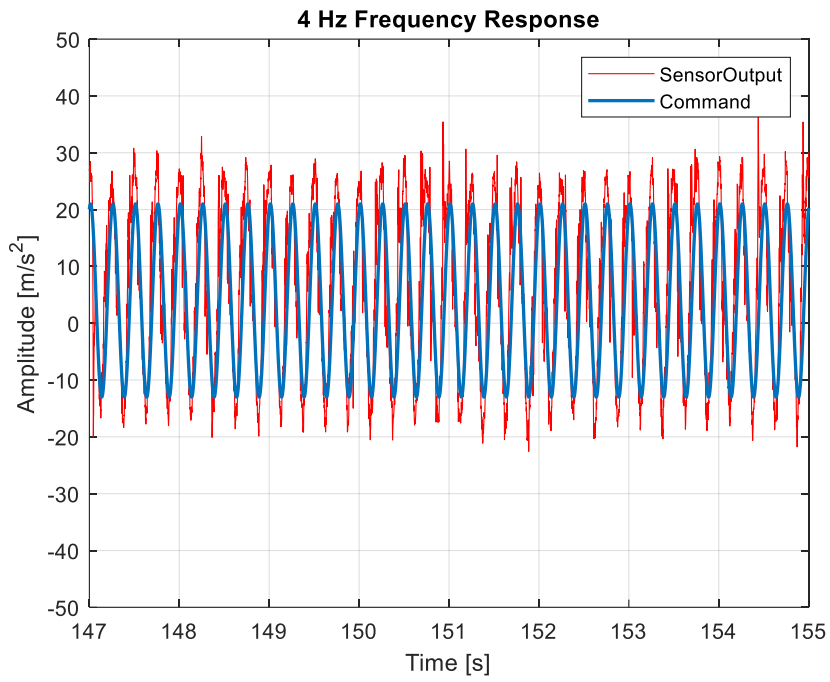
(a)



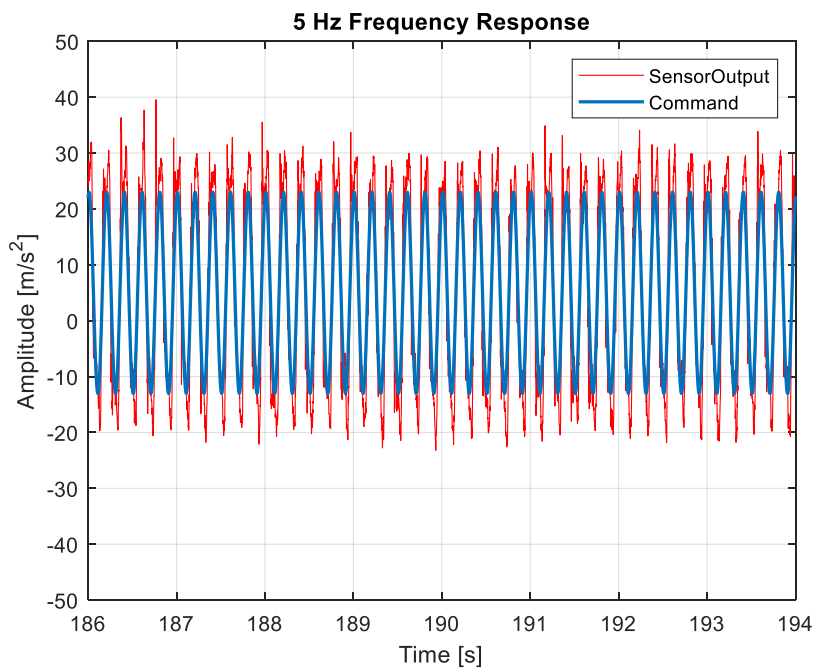
(b)



(c)



(d)



(e)

Figure 4.17. Frequency responses

From these frequency responses, one can draw the bode plot. It is drawn onto simulation result bode plot to give a comparison. It can be seen in Figure 4.18 where the blue one is simulation result and the red ones are the test results.

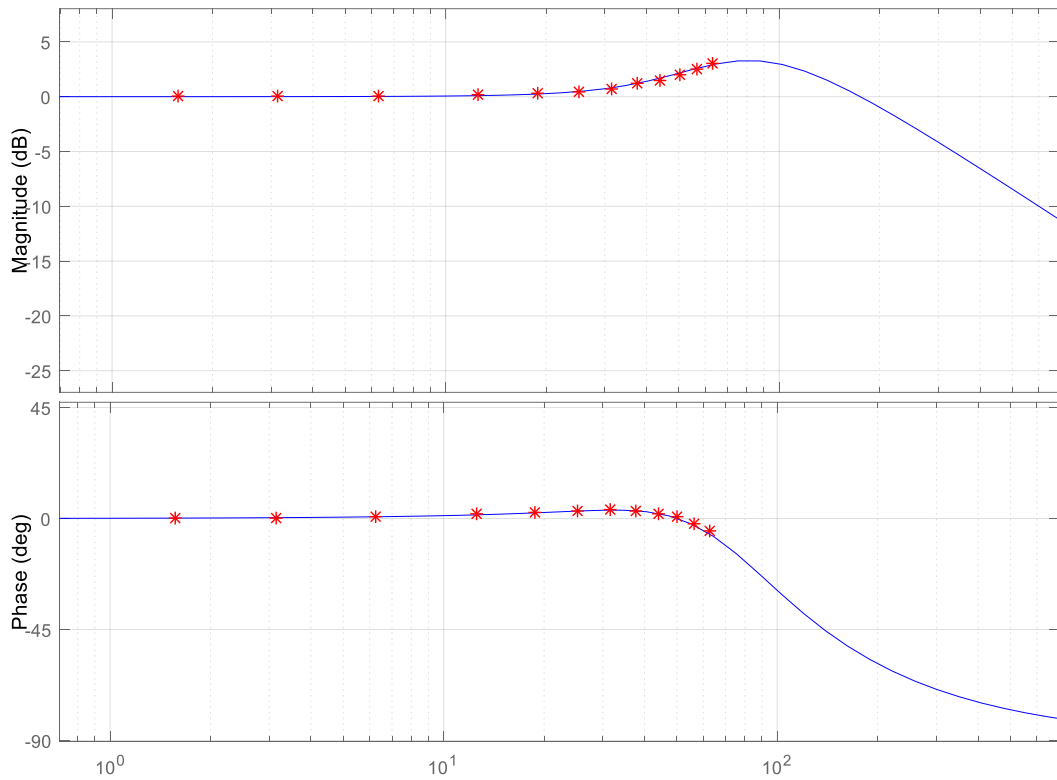


Figure 4.18. Bode plot comparison between simulation and test results.

CHAPTER 5

SUMMARY, CONCLUSION AND FUTURE WORK

5.1. Summary of Thesis

In this thesis study, an accelerometer is designed by implementing magnetic levitation principles. By levitating the proof mass, it is aimed to benefit for contactless sensing technology. Contactless sensors have a great potential to achieve superior performance and longer lifetime due to reduction in friction and absence of wear. Furthermore, it is expected to reach higher speed in other applications such as bearingless motors or gyroscopes etc. without mechanical contact.

A stable magnetic levitation cannot be achieved by only using permanent magnets as mentioned in Chapter 2. Therefore, active control must be implemented in a system, which uses magnetic levitation principles. In order to achieve a levitation in the system, active magnetic bearing concept should be studied. Equations are derived to model the magnetic bearing action in Chapter 2. At the end of the chapter, the reason why the system is inherently unstable is described. There is an unstable force component due to displacement of the rotor. It is also described in block diagram form.

After studying the magnetic bearing principles, the designed accelerometer is constructed and electronic hardware is combined to the system. A mathematical model of the system is derived and simulated in Simulink. The force factors are gathered from finite element analysis in Maxwell. Dimensions and necessary lengths are collected from 3D CAD of the test setup, which is drawn in Solidworks. Then, a PID controller is added and parameters are examined to get an effective output from the system.

To be able to conduct the experiments, a software should be designed in Simulink and deployed into DSP. This software is used to collect and filter the feedback signals from position sensors and current sensors. The position of the rotor is stabilized with the implemented PID controller. There is also communication blocks in the software to ease the parameter setting and collection of test signals.

PID parameters are tuned with the collected experimental data and the response of the system is presented in Chapter 4. Moreover, a comparison is made with a commercial sensor, which is STIM300 inertial sensor unit. The output of the designed accelerometer is compared with the acceleration output of STIM300 and the figures are shown for both axes under different disturbances. The maximum measurable acceleration value with the designed sensor is 0.6 g. The measurement limit is tested by rotating the test setup. Beyond 0.6 g level, electromagnetic actuators cannot levitate the rotor due to weight of it.

At the end of Chapter 4, an Allan Variance plot is drawn for STIM300 and also for designed setup. Random walk and bias instability values are detected from this figures and compared with the datasheet of STIM300. Allan Variance plot of the test setup shows the dynamic performance of the designed accelerometer. The result is comparably similar with the commercial sensor.

5.2. Conclusion of the Study

An accelerometer is designed and constructed at the end of the study. It shows that the magnetic levitation is a preferable way to achieve contactless devices. By introducing contactless sensors, the potential of the high performance measurements is increased. Moreover, the size of the devices can be decreased and the lifetime can be increased with contactless design.

The experimental results show the performance of the designed accelerometer. Results are highly encouraging to carry forward the design. The accelerometer measurements

from test setup is similar with the commercial sensor with 5-6 Hz disturbances. The designed accelerometer can be used to measure ± 0.6 g acceleration whereas the commercial sensor can measure ± 1.7 g. The bias instability of the accelerometer is 0.174 mg and random walk is 0.182 m/s/ \sqrt{h} .

5.3. Future Work

The magnetic analysis show that the generated magnetic force on the rotor can be increased with decreased air gap. By reducing the air gap between rotor and the electromagnetic actuator, bias current to levitate the rotor is increase. Therefore, the temperature of the solenoids is increased with the current because a readily purchased solenoid is used. A bigger electromagnetic actuator with bigger inner core and higher number of winding may be used to enhance magnetic force. Then, the size of the test setup would be bigger than the current design.

In this study, neodymium magnets are placed to above of electromagnets to not only control the radial position but also to control the levitation of the rotor. On the other hand, it is discussed to place the neodymium magnets in between the electromagnetic actuators to achieve higher force capability. Then, the system needs another actuator to stabilize the vertical axis. Moreover, the vertical axis would be highly unstable with this type of a design.

Furthermore, the accelerometer design can be move forward to design a magnetically levitated gyroscope by rotating the rotor of the sensor. By this way, angular velocity can be measured also by detecting the gyroscopic force value on the rotor.

REFERENCES

- [1] Oxford University Press, “Oxford Dictionaries,” *Oxford University Press*, 2019. .
- [2] S. Palagummi and F. G. Yuan, “Magnetic levitation and its application for low frequency vibration energy harvesting,” in *Structural Health Monitoring (SHM) in Aerospace Structures*, 2016, pp. 213–251.
- [3] SKF Group, “SKF S2M Magnetic Bearings for the oil and gas industry,” p. 1, 2016.
- [4] Y. MARUYAMA, T. MIZUNO, Y. ISHINO, M. TAKASAKI, T. ISHIGAMI, and H. KAMENO, “21620 Micro Gyroscopic Sensor using Active Magnetic Bearing : 3rd Report: Estimation of Tow-axis Angular Velocity Measurement in Frequency Domain,” *Proc. Conf. Kanto Branch*, 2017.
- [5] C. Zwyssig, T. Baumgartner, and J. W. Kolar, “High-speed magnetically levitated reaction wheel demonstrator,” in *2014 International Power Electronics Conference, IPEC-Hiroshima - ECCE Asia 2014*, 2014.
- [6] F. Barrot, “Acceleration and Inclination Sensors Based on Magnetic Levitation . Application in the Particular Case of Structural Health Monitoring in Civil Engineering,” *ÉCOLE POLYTECHNIQUE FÉDÉRALE DE LAUSANNE*, 2008.
- [7] M. Kraft, “Micromachined inertial sensors: The state-of-the-art and a look into the future,” in *Measurement and Control*, 2000, pp. 164–168.
- [8] R. F. YAZICIOĞLU, “SURFACE MICROMACHINED CAPACITIVE ACCELEROMETERS USING MEMS TECHNOLOGY,” *THE MIDDLE EAST TECHNICAL UNIVERSITY*, 2003.

- [9] J. Fraden, *Handbook of modern sensors: Physics, designs, and applications*. 2016.
- [10] J. S. Wilson, *Sensor Technology Handbook*. 2005.
- [11] A. Ito, "Servo type accelerometer," *The Journal of the Acoustical Society of America*, 2005. [Online]. Available: <https://www.imv.co.jp/e/products/vibrograph/pickup/servo/>. [Accessed: 02-Aug-2019].
- [12] H. BLEULER, "A Survey of Magnetic Levitation and Magnetic Bearing Types.," *JSME Int. journal. Ser. 3, Vib. Control Eng. Eng. Ind.*, 2012.
- [13] J. C. Maxwell, *A treatise on electricity and magnetism / Vol. 1*. 1873.
- [14] G. Schweitzer and E. H. Maslen, *Magnetic bearings: Theory, design, and application to rotating machinery*. 2009.
- [15] A. Chiba, T. Fukao, O. Ichikawa, M. Oshima, M. Takemoto, and D. G. Dorrell, *Magnetic Bearings and Bearingless Drives*. 2005.
- [16] G. Schweitzer, "Applications and research topics for active magnetic bearings," in *IUTAM Bookseries*, 2011.
- [17] Eclipse, "Eclipse Magnetics Catalogue." [Online]. Available: http://www.eclipsemagnetics.com/media/wysiwyg/brochures/ETNA/ETNA_catalogue_print_1.pdf. [Accessed: 01-Aug-2019].
- [18] Manyet, "Neodyum miknatis." [Online]. Available: <https://www.manyet.com/wp-content/uploads/2017/02/Neodyum-teknik-foy.pdf>. [Accessed: 01-Aug-2019].
- [19] TRsystems GmbH, "Eddy Current Sensor." [Online]. Available: https://www.unidor.info/gb-uk/downloads/wsd_s210mf_eng.pdf. [Accessed:

03-Aug-2019].

- [20] Lion Precision, “Differences Between Capacitive and Eddy-Current Sensors,” p. 9, 2009.
- [21] Texas Instruments, “C2000 Delfino MCUs F28377S LaunchPad Development Kit,” 2019. [Online]. Available: <http://www.ti.com/tool/LAUNCHXL-F28377S#0>. [Accessed: 03-Mar-2019].
- [22] Texas Instruments, “TMS320F2837xS Delfino™ Microcontrollers.” 2014.
- [23] Texas Instruments, “C2000 Delfino MCU F28379D LaunchPad™ development kit,” 2019. [Online]. Available: <http://www.ti.com/tool/LAUNCHXL-F28379D>. [Accessed: 03-Mar-2019].
- [24] T. Instruments, “TMS320F28379D Delfino™ Microcontrollers,” no. August, 2016.
- [25] Pololu, “Dual MC33926 Motor Driver Carrier.” [Online]. Available: <https://www.pololu.com/product/1213/pictures>. [Accessed: 14-May-2019].
- [26] Sensoror AS, “Ultra - High Performance Inertial Measurement Unit (Imu) - STIM300,” p. 2, 2011.
- [27] M. Matejcek and M. Sostronek, “New experience with Allan variance: Noise analysis of accelerometers,” in *2017 9th International Scientific Conference on Communication and Information Technologies, KIT 2017 - Proceedings*, 2017.

APPENDICES

A. Script for Allan Variance

```
close all

t0=1/1000;
theta = cumsum(signal)*t0;

maxNumM = 100;
L = size(theta, 1);
maxM = 2.^floor(log2(L/2));
m = logspace(log10(1), log10(maxM), maxNumM).';
m = ceil(m); % m must be an integer.
m = unique(m); % Remove duplicates.

tau = m*t0;
avar = zeros(numel(m), 1);
for i = 1:numel(m)
    mi = m(i);
    avar(i,:) = sum( ...
        (theta(1+2*mi:L) - 2*theta(1+mi:L-mi) +
theta(1:L-2*mi)).^2, 1);
end
avar = avar ./ (2*tau.^2 .* (L - 2*m));

adev = sqrt(avar);

figure
loglog(tau(1:78), adev(1:78))
title('Allan Deviation')
xlabel('\tau');
ylabel('\sigma(\tau)')
grid on
axis equal
% ylim([1e-5 1])
% xlim([1e-3 20])
```

```

% Find the index where the slope of the log-scaled
Allan deviation is equal
% to the slope specified.
slope = -0.5;
logtau = log10(tau);
logadev = log10(adev);
dlogadev = diff(logadev) ./ diff(logtau);
[~, i] = min(abs(dlogadev - slope));

% Find the y-intercept of the line.
b = logadev(i) - slope*logtau(i);

% Determine the angle random walk coefficient from
the line.
logN = slope*log(1) + b;
N = 10^logN;
N_inms = 10^logN*9.81*60 % convert from mg to m/s
% Plot the results.
tauN = 1;
lineN = N ./ sqrt(tau);
figure
loglog(tau, adev, tau, lineN, '--', tauN, N, 'o')
title('Allan Deviation with Angle Random Walk')
xlabel('\tau')
ylabel('\sigma(\tau)')
legend('\sigma', '\sigma_N')
text(tauN, N, 'N')
grid on
axis equal

```

```

% Find the index where the slope of the log-scaled
Allan deviation is equal
% to the slope specified.
slope = 0.5;
logtau = log10(tau);
logadev = log10(adev);
dlogadev = diff(logadev) ./ diff(logtau);
[~, i] = min(abs(dlogadev - slope));

```

```

% Find the y-intercept of the line.
b = logadev(i) - slope*logtau(i);

% Determine the rate random walk coefficient from
the line.
logK = slope*log10(3) + b;
K = 10^logK

% Plot the results.
tauK = 3;
lineK = K .* sqrt(tau/3);
figure
loglog(tau, adev, tau, lineK, '--', tauK, K, 'o')
title('Allan Deviation with Rate Random Walk')
xlabel('\tau')
ylabel('\sigma(\tau)')
legend('\sigma', '\sigma_K')
text(tauK, K, 'K')
grid on
axis equal

% Find the index where the slope of the log-scaled
Allan deviation is equal
% to the slope specified.
slope = 0;
logtau = log10(tau);
logadev = log10(adev);
dlogadev = diff(logadev) ./ diff(logtau);
[~, i] = min(abs(dlogadev - slope));

% Find the y-intercept of the line.
b = logadev(i) - slope*logtau(i);

% Determine the bias instability coefficient from
the line.
scfB = sqrt(2*log(2)/pi);
logB = b - log10(scfB);
B = 10^logB

```

```

% Plot the results.
tauB = tau(i);
lineB = B * scfB * ones(size(tau));
figure
loglog(tau, adev, tau, lineB, '--', tauB, scfB*B,
'o')
title('Allan Deviation with Bias Instability')
xlabel('\tau')
ylabel('\sigma(\tau)')
legend('\sigma', '\sigma_B')
text(tauB, scfB*B, '0.664B')
grid on
axis equal

```

```

tauParams = [tauN, tauB];
params = [N, scfB*B];
figure
loglog(tau(1:78), adev(1:78), tau(1:78),
[lineN(1:78), lineB(1:78)], '--', ...
tauParams, params, 'o')
title('Allan Deviation with Noise Parameters')
xlabel('\tau')
ylabel('\sigma(\tau)')
legend('\sigma', '\sigma_N', '\sigma_B')
text(tauParams, params, {'N', '0.664B'})
grid on
axis equal

```